

Electromagnetic Probes

Rupa Chatterjee, Lusaka Bhattacharya, and Dinesh K. Srivastava

Abstract We introduce the seminal developments in the theory and experiments of electromagnetic probes for the study of the dynamics of relativistic heavy-ion collisions and quark–gluon plasma.

1 Introduction

Collision of heavy nuclei at relativistic energies is expected to lead to formation of a deconfined state of matter known as quark–gluon plasma (QGP) [1], where quarks and gluons are the effective degrees of freedom rather than nucleons or hadrons [2, 3]. It is now well accepted that a few microseconds after the “Big Bang,” the whole universe was in the state of QGP [4].

Several experiments performed at the super proton synchrotron (SPS) at CERN and relativistic heavy-ion collider (RHIC) at Brookhaven National Laboratory, New York, have provided a significant evidence of the formation of this novel state of matter. A giant accelerator known as large hadron collider (LHC) at CERN will be in operation very soon and will provide many new insights about the properties of QGP and the theory of strong interactions.

Heavy-ion collisions at relativistic energies produce extremely high temperatures and energy densities within a very small volume. As a result, quarks and gluons (also known as partons) no longer remain confined within the nucleonic volume and create a deconfined state of partons due to multiple scatterings and production of secondaries due to gluon multiplications. The system (or the fireball) may reach a state of local thermal equilibrium. It cools by expansion and below a certain critical temperature ($T_c \sim 180$ MeV) or energy density, the partons are confined to form

R. Chatterjee (✉)

Variable Energy Cyclotron Centre, Kolkata 700064, India, rupa@veccal.ernet.in

L. Bhattacharya

Saha Institute of Nuclear Physics, Kolkata 700064, India,
lusaka.bhattacharya@saha.ac.in

D.K. Srivastava

Variable Energy Cyclotron Centre, Kolkata 700064, India, dinesh@veccal.ernet.in

hadrons and the system reaches a hadronic state. It may undergo a further expansion and cooling before the freeze-out takes place.

Radiation of photons and dileptons has been proposed as the most promising and efficient tool to characterize the initial state of heavy-ion collisions. Unlike hadrons, which are emitted from the freeze-out surface after undergoing intense re-scatterings, photons come out from each and every phase of the expanding fireball. Being electromagnetic in nature, they interact only weakly and their mean free path is larger than the typical system size (~ 10 fm). As a result once produced, they do not suffer further interaction with the medium ($\alpha \ll \alpha_s$) and carry undistorted information about the circumstances of their production to the detector [5].

Initially, photons (real as well as virtual) were studied in order to get only the temperature of the plasma. Several other possibilities, e.g., (i) evolution of the system size by intensity interferometry [6–9], (ii) momentum anisotropy of the initial partons [10, 11] as well as formation time of quark–gluon plasma [12] using elliptic flow of thermal photons, (iii) an accurate check on jet quenching and other aspects of the collision dynamics by photons due to passage of high-energy jets through plasma [13], have come to the fore. Of course dileptons are considered as the most reliable messengers of the medium modification of vector mesons [14].

2 Sources of Photons

In order to proceed, it is useful to identify various sources of photons from relativistic heavy-ion collisions. Their production is a result of convolution of the emissions from the entire history of the nuclear collision. Photons are emitted from the pre-equilibrium stage, from QGP phase, from hadronic phase, and also from the decay

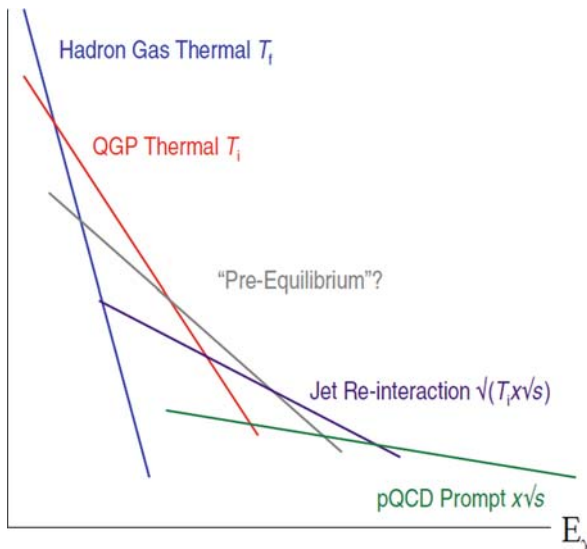


Fig. 1 Schematic diagram of different sources of photons and their relative p_T spectra

of hadrons produced at the time of freeze-out. An ideal situation would ensue if the contributions from different stages dominate different parts of the p_T spectrum. A schematic diagram of the different sources of photons and their slopes is shown in Fig. 1. We, thus, need rates and models to study the evolution from different sources. Hydrodynamics, cascade, fireball, cascade+hydrodynamics are the vastly used models for this purpose.

2.1 Direct Photons

The term “direct photons” stands for the photons which emerge directly from a particle collision. In a heavy-ion collision experiment, the detector captures all the emitted photons including those from decay of final state hadrons. The resultant spectrum is the inclusive photon spectrum. However, more than 90% of the photons in this spectrum are from hadron decay. One can subdivide this broad category of “direct photons” into “prompt,” “pre-equilibrium,” “thermal” (from QGP as well as hadronic phase), and “jet conversion” depending on their origin. Before we come to the different sub-categories of direct photons, we start our discussion with decay photons and their subtraction from the inclusive photon spectrum.

2.2 Decay Photons

As mentioned earlier, most of the decay photons are from 2γ decay of π^0 and η mesons. ω , η' , etc., also contribute to the decay photon spectrum, marginally. Subtraction of the decay background from inclusive photon spectrum is a very challenging task. WA98 Collaboration [15] used the subtraction method using invariant mass analysis for decay background and later PHENIX Collaboration [16] has developed this method to a much higher level of sophistication.

2.2.1 Invariant Mass Analysis

Extraction of direct photon spectrum from the inclusive photon spectrum is done using invariant mass analysis as the primary step. First, all the detected photons are listed on an event-by-event basis. Then by selecting two photons randomly from an event, invariant mass of the pair is calculated. If E_1 , E_2 are the energies and \mathbf{p}_1 , \mathbf{p}_2 are the three momenta of the photons respectively, then the invariant mass of the pair is

$$M_{\gamma\gamma} = [(E_1 + E_2)^2 - (\mathbf{p}_1 + \mathbf{p}_2)^2]^{1/2}. \quad (1)$$

If the value of $M_{\gamma\gamma}$ is close to m_{π^0} , it is assumed that they are the decay products from the same pion and a π^0 spectrum is obtained. Similarly the η spectrum is obtained. These two spectra are then used to determine the decay photon spectrum

using kinematics and the subtraction of this spectrum from the inclusive spectrum gives the direct photon spectrum.

However, in an event having N number of photons, the total number of photon pairs that can be formed is ${}^N C_2$. For large values of N , this number gets very large. Thus, there is a very high probability of getting a pair of photons having an invariant mass m_{π^0} or m_η , which are not decay products of the same pion or η meson.

Several other issues also need to be accounted for: (i) the detector resolution is finite, (ii) the opening angle between the decay photons can get very small, especially if the energy of the pion is large, (iii) the photons may not deposit all their energy in the detector, and (iv) one of the photons may be outside the coverage of the detector.

2.2.2 Mixed-Event Analysis

Thus, the major problem of invariant mass analysis is that the accidental (false) photon pairs can also give rise to pion mass and it is not possible to distinguish them from the correlated pairs. To overcome this problem, a mixed-event analysis [17] procedure has been used successfully. The basic idea of mixed-event technique is

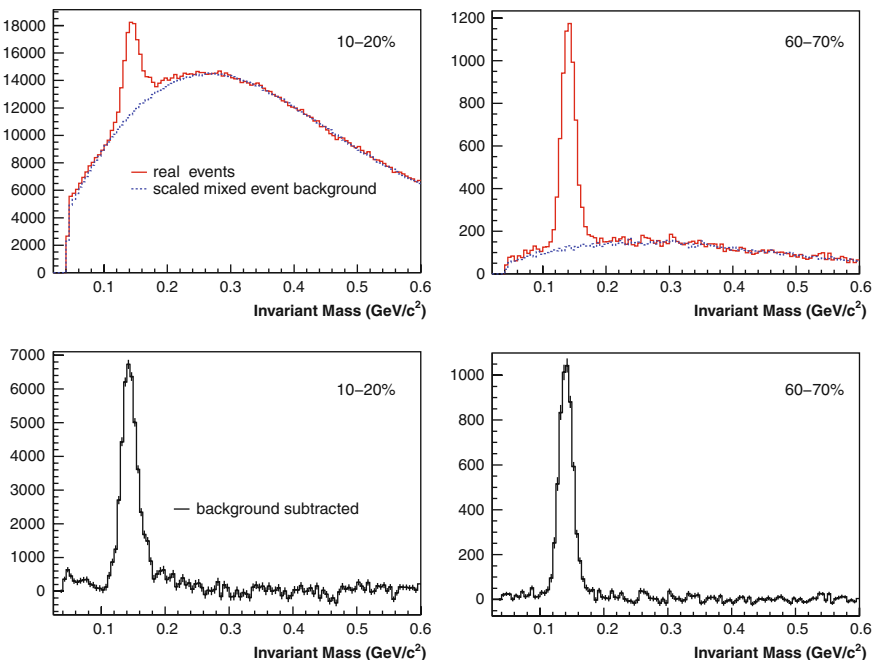


Fig. 2 Invariant mass distributions of pairs of electromagnetic clusters passing photon selection cuts for pair transverse momenta satisfying $3.0 < p_T < 3.5$ GeV. Top panels: $m_{\gamma\gamma}$ distributions in Au+Au events compared to a normalized mixed-event sample representing the combinatoric background. Bottom panels: The $m_{\gamma\gamma}$ distributions after subtraction of the combinatoric background for 10–20 and 60–70% centrality bins [17]

to compare particle spectrum from one event to the result for particle combinations from different events, which are a priori not correlated. As a first step, properly normalized mixed events are constructed by randomly sampling photons from different events. The difference of the invariant mass spectra (see Fig. 2) of the real events and the mixed events then gives the pion and η distributions. Once again, the decay photon spectrum is subtracted from the inclusive photon spectrum to get the direct photons.

2.2.3 Internal Conversion and Tagging of Decay Photons

An alternative approach of separating direct photons from decay background is by measuring the “quasi-real” virtual photons which appear as low mass electron–positron pair. It is assumed that any source of real photons also produces low mass virtual photons which decay into e^+e^- pair. This method is known as internal conversion method [18, 19] and is based on two assumptions. The first assumption is that the ratio of direct to inclusive photons is the same for real as well as virtual photons having $m_\gamma < 30$ MeV, i.e., $\gamma_{\text{dir}}^*/\gamma_{\text{incl}}^* = \gamma_{\text{dir}}/\gamma_{\text{incl}}$. Second, the mass distribution follows the Kroll–Wada formula [20]:

$$\frac{d^2n_{ee}}{dm_{ee}} = \frac{2\alpha}{3\pi} \frac{1}{m_{ee}} \sqrt{1 - \frac{4m_e^2}{m_{ee}^2}} \left(1 + \frac{2m_e^2}{m_{ee}^2}\right) S dn_\gamma. \quad (2)$$

Here, m_e and m_{ee} are the masses of electron and e^+e^- pair, respectively, and α is the fine structure constant. This method is used for Compton scattering ($q + g \rightarrow q + \gamma^* \rightarrow q + e^+ + e^-$), Dalitz decay ($\pi^0, \eta \rightarrow e^+e^-\gamma$, $\omega \rightarrow e^+e^-\pi^0$), and also for two γ decay of several other hadrons. The factor S in Eq. (2) is process dependent and for π^0 ($\rightarrow \gamma\gamma^* \rightarrow \gamma e^+e^-$) decay it is expressed as [21]

$$S = |F(m_{ee}^2)|^2 \left(1 - \frac{m_{ee}^2}{M_h^2}\right)^3, \quad (3)$$

where M_h is the hadron mass and $F(m_{ee}^2)$ is the form factor. The factor S is 0 for $m_{ee} > M_h$ and goes to 1 as $m_{ee} \rightarrow 0$ or $m_{ee} \ll p_T$. The key advantage of this method is the greatly improved signal to background ratio which is achieved by elimination of the contribution of Dalitz (π^0) decay. The experimentally measured quantity is the ratio of e^+e^- pairs in a particular invariant mass bin and the direct photon spectrum is obtained by multiplying $\gamma_{\text{dir}}^*/\gamma_{\text{incl}}^*$ to the measured inclusive photon spectrum (left panel of Fig 3).

Due to the excellent resolution of the PHENIX detector to measure charged particles at low momenta, another powerful technique known as “tagging of decay photons” [22, 23] is used to eliminate the π^0 decay background. This method is very useful in the low and intermediate p_T range ($1 < p_T < 5$ GeV) as the systematic uncertainties introduced by detector efficiency, acceptance, etc., cancel out for measuring γ/γ_{π^0} directly in place of conventional double ratio

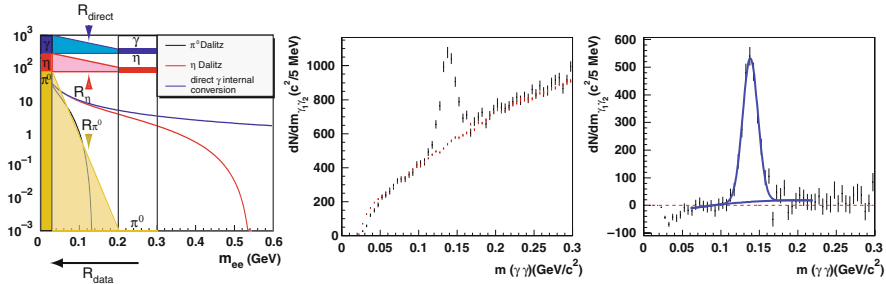


Fig. 3 *Left panel:* Invariant mass distribution of virtual photons from π^0 and η Dalitz decay as well as from direct photons [18, 19]. *Middle and right panels:* Invariant mass spectrum in “tagging” of decay photon method [22, 23]

($R = (\gamma/\pi^0)_{\text{measured}}/(\gamma/\pi^0)_{\text{decay}}$) technique. In this method, the invariant mass ($m_{\gamma e^+ e^-}$) distribution of the π^0 ($\rightarrow \gamma\gamma^* \rightarrow \gamma e^+ e^-$) decay products is constructed and then mixed-event analysis is used for the final subtraction (middle and right panel of Fig. 3).

2.3 Sources of Direct Photons

Direct photons can be classified into different categories depending on their origin from different stages of the expanding fireball formed after the collision. These are (1) prompt photons, which originate from initial hard scatterings, (2) pre-equilibrium photons, produced before the medium gets thermalized, (3) thermal photons from quark–gluon plasma as well as by hadronic reactions in the hadronic phase, and (4) photons from passage of jets through plasma. It is not possible experimentally to distinguish between the different sources. Thus, theory can be used with a great advantage to identify these sources of direct photons and their relative importance in the spectrum [24].

2.3.1 Partonic Processes for Production of Prompt Photons

In relativistic heavy-ion collisions, prompt photons are produced due to quark–gluon Compton scattering ($q + g \rightarrow q + \gamma$), quark–antiquark annihilation process ($q + \bar{q} \rightarrow g + \gamma$), and quark fragmentation ($q \rightarrow q + \gamma$) following scattering of partons of the nucleons in the colliding nuclei (see Fig. 4). At lowest order in $\alpha\alpha_s$, quark–gluon Compton scattering and quark–antiquark annihilation processes dominate the photon production. In next-to-leading order (NLO) calculation, many more complicated scattering processes appear in the photon production cross section and the total contribution can be written as addition of two different terms as [25]

$$\frac{d\sigma}{d\vec{p}_T d\eta} = \frac{d\sigma^{(D)}}{d\vec{p}_T d\eta} + \frac{d\sigma^{(F)}}{d\vec{p}_T d\eta}. \quad (4)$$

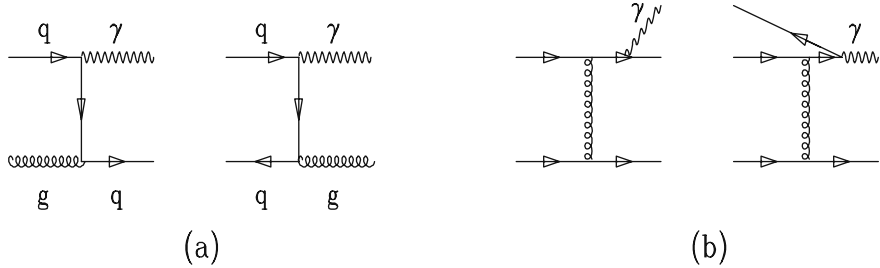


Fig. 4 Partonic processes for production of photons from (a) quark–gluon Compton scattering, quark–antiquark annihilation process, and (b) quark fragmentation

In the above equation “ D ” stands for “direct” or the total Compton scattering and annihilation contribution while the photons from fragmentation are denoted by “ F ”. It is clear that the “ D ” photons are well separated from hadrons. The “ F ” photons, on the other hand, have their origin in collinear fragmentation of colored high- p_T partons and are accompanied by hadrons. This can be used with advantage as the produced photons can be separated out by employing useful isolation cuts. The two terms in Eq. (4) can be written explicitly as [26]

$$\frac{d\sigma^{(D)}}{d\vec{p}_T d\eta} = \sum_{i,j=q,\bar{q},g} \int dx_1 dx_2 F_{i/h_1}(x_1, M) F_{j/h_2}(x_2, M) \frac{\alpha_s(\mu_R)}{2\pi} \times \left(\frac{d\hat{\sigma}_{ij}}{d\vec{p}_T d\eta} + \frac{\alpha_s(\mu_R)}{2\pi} K_{ij}^{(D)}(\mu_R, M, M_F) \right) \quad (5)$$

and

$$\frac{d\sigma^{(F)}}{d\vec{p}_T d\eta} = \sum_{i,j,k=q,\bar{q},g} \int dx_1 dx_2 \frac{dz}{z^2} F_{i/h_1}(x_1, M) F_{j/h_2}(x_2, M) D_{\gamma/k}(z, M_F) \times \left(\frac{\alpha_s(\mu_R)}{2\pi} \right)^2 \left(\frac{d\hat{\sigma}_{ij}^k}{d\vec{p}_T d\eta} + \frac{\alpha_s(\mu_R)}{2\pi} K_{ij,k}^{(F)}(\mu_R, M, M_F) \right). \quad (6)$$

Here, $F_{i/h_{1,2}}(x, M)$ are the parton distribution functions and $\alpha_s(\mu_R)$ is the strong coupling defined in the \overline{MS} renormalization scheme at the renormalization scale μ_R ; for details see [25]. As mentioned earlier, in a complete and consistent NLO pQCD [$O(\alpha\alpha_s^2)$] calculation, important contribution to prompt photon result arises from various possible $2 \rightarrow 3$ processes like $ab \rightarrow \gamma cd$ for the direct as well as for the fragmentation processes [26, 27].

In case of photons from fragmentation, the higher order correction is very important at low x_T ($= 2p_T/\sqrt{s}$). By choosing a scale for factorization, renormalization, and fragmentation, all equal to $p_T/2$, a very good quantitative description is obtained for all the available pp and $p\bar{p}$ data without introduction of any intrinsic

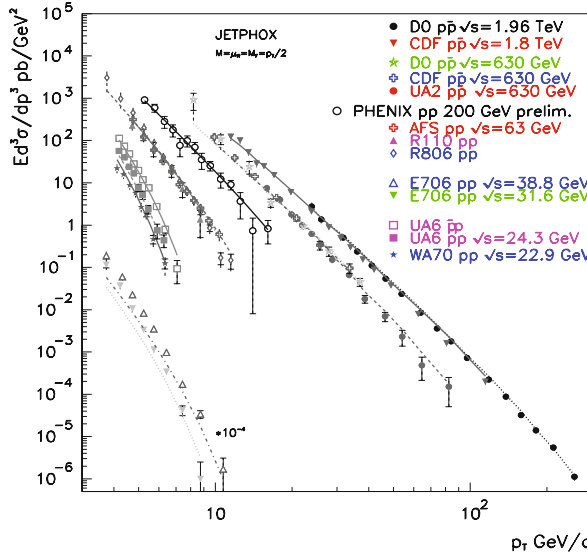


Fig. 5 World's inclusive and isolated direct photon production cross sections measured in pp and $p\bar{p}$ collisions compared to JETPHOX NLO predictions, using BFG II(CTEQ6M) for fragmentation (structure) functions and a common scale $p_T/2$ [25]

k_T . Results spanning over two orders of magnitude in energy and over nine orders of magnitude in cross sections are shown in Fig. 5.

It should be mentioned though that a similar exercise for pions requires a scale of $p_T/3$ [28].

In the early calculations, the results for nucleus–nucleus scatterings were often obtained by multiplying the pp results for some \sqrt{s} with corresponding scaling factor $N_{\text{coll}} (= \sigma_{NN} T_{AB})$; where σ_{NN} is the nucleon–nucleon cross section and T_{AB} is the nuclear overlapping function for nuclei A and B) or number of binary collisions. In actual practice, often enough, σ_{NN} was replaced by σ_{pp} . However, as the valence quark structures of protons (uud) and neutrons (udd) are different, one needs to correctly account for the iso-spin of the nucleons to calculate the prompt contribution. This correction will strongly affect the results in the p_T range, where the valence quark contribution is significant. Also, remember that there is no direct measurement for pn and nn cross sections, though they can be estimated by comparing results of scatterings involving deuterons. The effect of shadowing on structure function and energy loss of final state quarks before they fragment into hadrons are two other corrections [29, 30] which need to be accounted for.

In order to clearly see this point we show the results for prompt photons for nn and pn collisions normalized to those for pp collisions at $\sqrt{s} = 200$ GeV in the left panel of Fig. 6. It is clear that at low x_T (where processes involving gluons dominate) the effect is not very significant, however with larger values of x_T (where the processes involving valence quarks dominate), the production of photons decreases by a large factor for the case of pn and nn collisions.

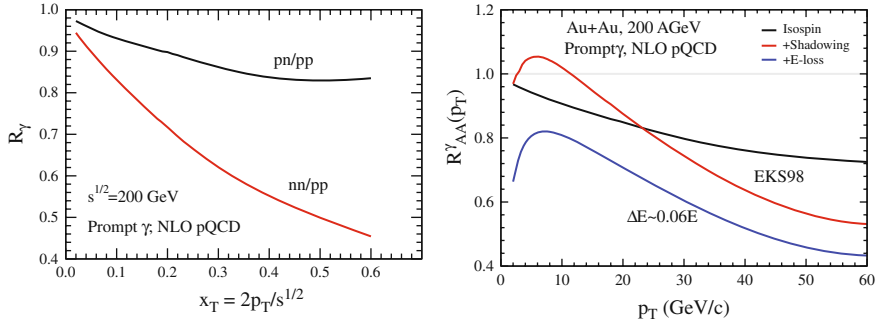


Fig. 6 *Left panel:* Prompt photons for $p\bar{n}$ and $n\bar{n}$ collisions normalized to those for $p\bar{p}$ collisions at $\sqrt{s} = 200$ GeV. *Right panel:* Iso-spin, shadowing, and energy loss corrected R_{AA}^γ for prompt photons at $200A$ GeV $Au+Au$ collisions using NLO pQCD

The transverse momentum-dependent nuclear modification factor R_{AA} defined as

$$R_{AA}(p_T) = \frac{1}{N_{coll}} \frac{d\sigma_\gamma^{AA}(p_T)/dyd^2p_T}{d\sigma_\gamma^{pp}(p_T)/dyd^2p_T} \quad (7)$$

for prompt photons using NLO pQCD and considering iso-spin, shadowing, and energy loss effects for $200A$ GeV $Au+Au$ collisions at RHIC is shown in the right panel of Fig. 6. We note that, for $p_T < 10$ GeV, the iso-spin and shadowing corrected result shows an enhancement in the prompt photon production compared to the situation when only the iso-spin correction is incorporated [31]. This is due to anti-shadowing for larger values of Bjorken x or large x_T . The inclusion of the energy loss pushes down the value of R_{AA} to less than 1 for all p_T . We also give a comparison with the PHENIX [32] experimental data in the bottom lower panel of Fig. 8.

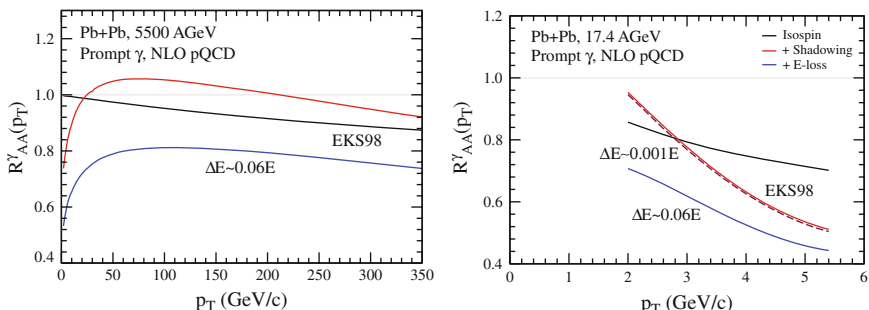


Fig. 7 Iso-spin, shadowing, and energy loss corrected R_{AA}^γ for prompt photons at LHC (*left panel*) and SPS (*right panel*) energies using NLO pQCD

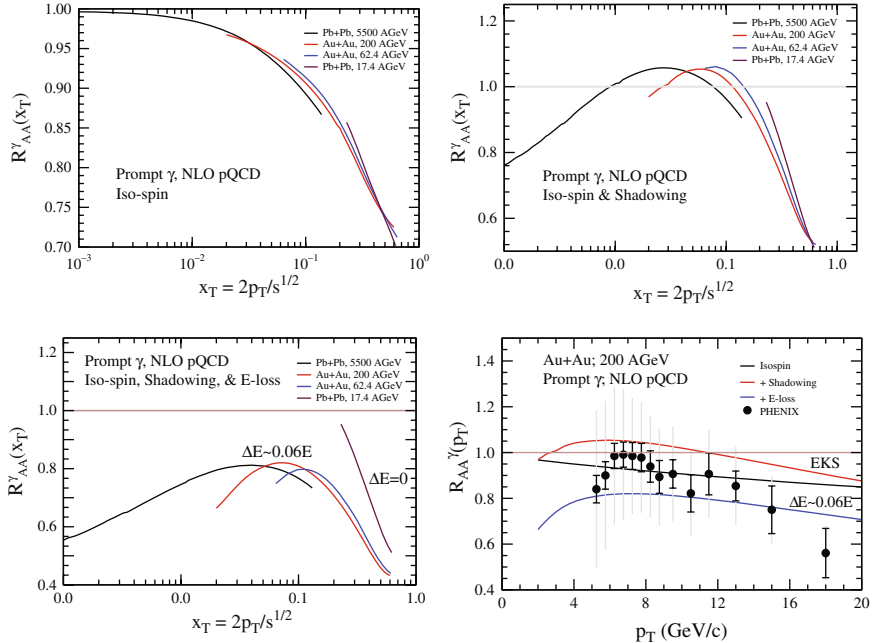


Fig. 8 Iso-spin, shadowing, and fragmentation energy-loss-corrected NLO pQCD results at different collider energies with different target projectile combination and comparison of the RHIC results with PHENIX [32] data

NLO results at LHC (Pb+Pb@ $5.5A$ TeV) and SPS (Pb+Pb@ $17.4A$ GeV) are shown in Fig. 7. To clearly demonstrate the relative features of iso-spin, shadowing, and energy-loss-corrected prompt photons at different collider energies, results for R_{AA} as function of x_T are shown in Fig. 8.

2.4 Photon Production from Quark–Gluon Plasma

The thermal emission rate of photons with energy E and momentum p from a small system (compared to the photon mean free path) is related to the imaginary part of the photon self-energy by the following relation:

$$E \frac{dR}{d^3 p} = \frac{-2}{(2\pi)^3} Im \Pi_\mu^{R,\mu} \frac{1}{e^{E/T} - 1}, \quad (8)$$

where $\Pi_\mu^{R,\mu}$ is the retarded photon self-energy at a finite temperature T . This relation is valid in the perturbative [33, 34] as well as non-perturbative [35] limits. It is also valid to all orders in the strong interactions and to order e^2 in the electromagnetic interactions. If the photon self-energy is approximated by carrying out a

loop expansion to some finite order, then the formulation of Eq. (8) is equivalent to relativistic kinetic theory. In order to illustrate this, we closely follow the treatment of [36, 37].

Thus using relativistic kinetic theory formulation, the contribution of these processes to the rate can be written as [36–38]

$$\begin{aligned} \mathcal{R}_i = \mathcal{N} \int \frac{d^3 p_1}{2E_1(2\pi)^3} \frac{d^3 p_2}{2E_2(2\pi)^3} f_1(E_1) f_2(E_2) (2\pi)^4 \delta(p_1^\mu + p_2^\mu - p_3^\mu - p^\mu) \\ \times |\mathcal{M}_i|^2 \frac{d^3 p_3}{2E_3(2\pi)^3} \frac{d^3 p}{2E(2\pi)^3} [1 \pm f_3(E_3)], \end{aligned} \quad (9)$$

where \mathcal{M}_i represents the amplitude for one of these processes and the f' s are the Fermi–Dirac or Bose–Einstein distribution functions as appropriate. Positive and negative signs in the last part of Eq. (9) correspond to Bose enhancement and Pauli suppression, respectively.

The integral above can be simplified by introducing Mandelstam variables $s = (p_1 + p_2)^2$, $t = (p_1 - p_3)^2$, and $u = (p_1 - p)^2$. Now the differential photon rate can be written as

$$\begin{aligned} E \frac{d\mathcal{R}_i}{d^3 p} = \frac{\mathcal{N}}{(2\pi)^7} \frac{1}{16E} \int ds dt |\mathcal{M}_i(s, t)|^2 \int dE_1 dE_2 f_1(E_1) f_2(E_2) \\ \times [1 \pm f_3(E_1 + E_2 - E)] \theta(E_1 + E_2 - E) (aE_1^2 + bE_1 + c)^{-1/2}, \end{aligned} \quad (10)$$

where

$$\begin{aligned} a &= -(s + t)^2, \\ b &= 2(s + t)(Es - E_2t), \\ c &= st(s + t) - (Es + E_2t)^2. \end{aligned} \quad (11)$$

Considering the photon energy to be large, one can consider $f_1(E_1)f_2(E_2) \approx e^{-(E_1+E_2)/T}$ and simplify the above as

$$E \frac{d\mathcal{R}_i}{d^3 p} = \frac{\mathcal{N}}{(2\pi)^6} \frac{T}{32E} e^{-E/T} \int \frac{ds}{s} \ln(1 \pm e^{-s/4ET})^{\pm 1} \int dt |\mathcal{M}_i(s, t)|^2. \quad (12)$$

In the above equation, positive and negative signs stand for fermions (q) and bosons (g) in the final state, respectively.

The relation between the amplitude and differential cross section for mass less particles can be written as

$$\frac{d\sigma}{dt} = \frac{|\mathcal{M}|^2}{16\pi s^2}. \quad (13)$$

And thus, the differential cross sections for annihilation process and Compton scattering are

$$\frac{d\sigma^{\text{annihilation}}}{dt} = \frac{8\pi\alpha\alpha_s}{9s^2} \frac{u^2 + t^2}{ut} \quad (14)$$

and

$$\frac{d\sigma^{\text{Compton}}}{dt} = \frac{-\pi\alpha\alpha_s}{3s^2} \frac{u^2 + s^2}{us}. \quad (15)$$

For annihilation process, $\mathcal{N} = 20$ when summing over u and d quarks and for Compton scattering, $\mathcal{N} = 320/3$. The total cross section can be obtained after integrating over t . These differential cross sections have a singularity at t and/or $u = 0$ and the total cross section is infinite as the processes involve exchange of massless particle.

To screen this divergence many-body effects are necessary. This approach will be discussed later. As a first step let us isolate the region of phase space causing the divergences. The integration is done over

$$-s + k_c^2 \leq t \leq -k_c^2, \quad 2k_c^2 \leq s \leq \infty, \quad (16)$$

where $T^2 \gg k_c^2 > 0$ is an infrared cutoff.

This treats u and t symmetrically and maintains the identity $s + t + u = 0$ appropriate for all massless particles.

In the limit that $k_c^2 \rightarrow 0$,

$$E \frac{d\mathcal{R}^{\text{Compton}}}{d^3 p} = \frac{5}{9} \frac{\alpha\alpha_s}{6\pi^2} T^2 e^{-E/T} [\ln(4ET/k_c^2) + C_F], \quad (17)$$

$$E \frac{d\mathcal{R}^{\text{annihilation}}}{d^3 p} = \frac{5}{9} \frac{\alpha\alpha_s}{3\pi^2} T^2 e^{-E/T} [\ln(4ET/k_c^2) + C_B], \quad (18)$$

where

$$C_F = \frac{1}{2} - C_{\text{Euler}} + \frac{12}{\pi^2} \sum_{n=2}^{\infty} \frac{(-1)^n}{n^2} \ln n = 0.0460 \dots, \quad (19)$$

$$C_B = -1 - C_{\text{Euler}} - \frac{6}{\pi^2} \sum_{n=2}^{\infty} \frac{1}{n^2} \ln n = -2.1472 \dots \quad (20)$$

These expressions use the full Fermi–Dirac or Bose–Einstein distribution functions in the final state.

These results have a very interesting structure. Thus, the factor $5/9$ arises from the sum of the squares of the electric charges of the u and d quarks, the factor $\alpha\alpha_s$ comes from the topological structure of the diagrams, a factor T^2 comes from phase

space which gives the overall dimension of the rate, and we have the Boltzmann factor $e^{-E/T}$ for photons of energy E . The logarithm arises due to the infrared behavior.

2.4.1 Infrared Contribution

The infrared divergence in the photon production rate [36, 37] discussed above is caused by a diverging differential cross section when the momentum transfer goes to zero. Oftentimes long-ranged forces can be screened by many-body effects at finite temperatures. Braaten and Pisarski have analyzed problems such as this one in QCD [39–41]. They have argued that a cure can be found in reordering perturbation theory by expanding correlation functions in terms of effective propagators and vertices instead of bare ones. These effective propagators and vertices are just the bare ones plus one-loop corrections, with the caveat that the one-loop corrections are evaluated in the high-temperature limit. This makes them relatively simple functions.

The analysis of Braaten and Pisarski shows that a propagator must be dressed if the momentum flowing through it is soft (small compared to T). This is because propagation of soft momenta is connected with infrared divergences in loops. Dressing of propagators are necessary, otherwise corrections due to these are also infinite.

Using the one-loop corrected propagators and vertices and the contribution to the rate coming from the infrared-sensitive part of phase space can be written as

$$E \frac{d\mathcal{R}^{\text{BP}}}{d^3 p} = \frac{5}{9} \frac{\alpha \alpha_s}{2\pi^2} T^2 e^{-E/T} \ln\left(\frac{k_c^2}{2m_q^2}\right), \quad (21)$$

where $2m_q^2 = \frac{1}{3}g^2T^2$.

Adding this contribution to those given by Eqs. (19) and (20), the final result can be written as

$$E \frac{d\mathcal{R}}{d^3 p} = \frac{5}{9} \frac{\alpha \alpha_s}{2\pi^2} T^2 e^{-E/T} \ln\left(\frac{2.912}{g^2} \frac{E}{T}\right). \quad (22)$$

This is independent of the cutoff k_c . Thus, the Braaten–Pisarski method has worked beautifully to shield the singularity encountered above. We also note that in kinetic theory calculation, the effective infrared cutoff is $k_c^2 = 2m_q^2$. In earlier works an infrared cutoff was often imposed by giving the exchanged quark an effective temperature-dependent mass.

These early results have been brought to a high degree of sophistication and results complete to leading order in α_s with inclusion of LPM effects are now available, which should be used for detailed calculation [42].

2.4.2 Photons from Passage of Jets Through QGP

The relativistic heavy-ion collisions at RHIC (and LHC) energies are marked by a large production of high-energy quark and gluon jets which lose energy while

passing through the QGP due to collision and radiation of gluons. This is the celebrated phenomenon of jet quenching. A quark jet having a transverse momentum p_T would be formed within $\tau \sim 1/p_T$ which can be much smaller than τ_0 , when QGP is formed, for large p_T . This quark (or antiquark) jet, while passing through QGP may annihilate with a thermal antiquark (or quark) or undergo a Compton scattering with a thermal gluon and lead to production of a high-energy photon. This process is called the jet-photon conversion [13].

We have seen that the kinematics of the annihilation of a quark–antiquark pair ($q + \bar{q} \rightarrow \gamma + g$) is expressed in terms of the Mandelstam variables $s = (p_q + p_{\bar{q}})^2$, $t = (p_q - p_\gamma)^2$, and $u = (p_{\bar{q}} - p_\gamma)^2$. We also recall that the largest contribution to the production of photons arises from small values of t or u , corresponding to $p_\gamma \sim p_q$ or $p_\gamma \sim p_{\bar{q}}$ [2, 13, 43].

The phase-space distribution of the quarks and gluons produced in a nuclear collision can be approximately decomposed into two components, a thermal component f_{th} characterized by a temperature T and a hard component f_{jet} given by hard scattering of the partons and limited to transverse momenta $p_T \gg 1$ GeV: $f(\mathbf{p}) = f_{\text{th}}(\mathbf{p}) + f_{\text{jet}}(\mathbf{p})$. f_{jet} dominates for large momenta, while at small momenta f is completely given by the thermal part.

The phase-space distribution for the quark jets propagating through the QGP is given by the perturbative QCD result for the jet yield [13]:

$$f_{\text{jet}}(\mathbf{p}) = \frac{1}{g_q} \frac{(2\pi)^3}{\pi R_\perp^2 \tau p_T} \frac{dN_{\text{jet}}}{d^2 p_T dy} R(r) \delta(\eta - y) \Theta(\tau_{\max} - \tau_i) \Theta(R_\perp - r), \quad (23)$$

where $g_q = 2 \times 3$ is the spin and color degeneracy of the quarks, R_\perp is the transverse dimension of the system, and the η is the space–time rapidity. $R(r)$ is a transverse profile function. τ_{\max} is the smaller of the lifetime τ_f of the QGP and the time τ_d taken by the jet produced at position \mathbf{r} to reach the surface of the plasma.

One can approximate the invariant photon differential cross sections for the annihilation process and Compton scattering as [2, 13]

$$E_\gamma \frac{d\sigma^{(a)}}{d^3 p_\gamma} \sim \sigma^{(a)}(s) \frac{1}{2} E_\gamma [\delta(\mathbf{p}_\gamma - \mathbf{p}_q) + \delta(\mathbf{p}_\gamma - \mathbf{p}_{\bar{q}})] \quad (24)$$

and

$$E_\gamma \frac{d\sigma^{(C)}}{d^3 p_\gamma} \sim \sigma^{(C)}(s) E_\gamma \delta(\mathbf{p}_\gamma - \mathbf{p}_q). \quad (25)$$

Here, $\sigma^{(a)}(s)$ and $\sigma^{(C)}(s)$ are the corresponding total cross sections.

Using Eqs. (24) and (25), the rate of production of photons due to annihilation and Compton scattering is given by [2]

$$E_\gamma \frac{dN^{(a)}}{d^4x d^3 p_\gamma} = \frac{16E_\gamma}{2(2\pi)^6} \sum_{q=1}^{N_f} f_q(\mathbf{p}_\gamma) \int d^3 p f_{\bar{q}}(\mathbf{p}) [1 + f_g(\mathbf{p})] \sigma^{(a)}(s) \times \frac{\sqrt{s(s - 4m^2)}}{2E_\gamma E} + (q \leftrightarrow \bar{q}) \quad (26)$$

and

$$E_\gamma \frac{dN^{(C)}}{d^4x d^3 p_\gamma} = \frac{16E_\gamma}{(2\pi)^6} \sum_{q=1}^{N_f} f_q(\mathbf{p}_\gamma) \int d^3 p f_g(\mathbf{p}) [1 - f_q(\mathbf{p})] \sigma^{(C)}(s) \times \frac{(s - m^2)}{2E E_\gamma} + (q \rightarrow \bar{q}). \quad (27)$$

The f' s are the distribution functions for the quarks, antiquarks, and gluons. Inserting thermal distributions for the gluons and quarks one can obtain an analytical expression for these emission rates for an equilibrated medium [2, 36–38].

In order to estimate the jet-photon conversion contribution, we first note that the integrals over \mathbf{p} in Eqs. (26) and (27) are dominated by small momenta. Therefore dropping the jet part in the distributions, $f(\mathbf{p})$ in the integrands is approximated by the thermal part. Now performing the integrals and identifying the quark and antiquark distributions outside the integrals with the jet distributions, results for Compton and annihilation scatterings due to jet conversions are given as

$$E_\gamma \frac{dN_\gamma^{(a)}}{d^3 p_\gamma d^4 x} = E_\gamma \frac{dN_\gamma^{(C)}}{d^3 p_\gamma d^4 x} = \frac{\alpha \alpha_s}{8\pi^2} \sum_{f=1}^{N_f} \left(\frac{e_{q_f}}{e} \right)^2 [f_q(\mathbf{p}_\gamma) + f_{\bar{q}}(\mathbf{p}_\gamma)] T^2 \left[\ln \left(\frac{4E_\gamma T}{m^2} \right) + C \right]. \quad (28)$$

Here, $C = -1.916$. If we include three lightest quark flavors, then $\sum_f e_{q_f}^2/e^2 = 2/3$. We also assume that the mass m introduced here to shield the infrared divergence can be identified with the thermal quark mass m_{th} .

These pioneering works have now been corrected for energy loss and flavor change suffered by the jets, as they pass through the plasma [44] as well as bremsstrahlung induced by the passage of the jets through the plasma [45].

2.4.3 Equilibration Time for Photons

It is of interest to get an idea about the equilibration time of photons in the medium. Following the treatment of [36, 37], we note that the six-dimensional phase-space distribution $dn/d^3 p (= dN/d^3 x d^3 p)$ for the photons satisfies the rate equation:

$$\frac{d}{dt} \left(\frac{dn}{d^3 p} \right) = \frac{dR}{d^3 p} \left(1 - \frac{dn/d^3 p}{dn_{\text{eq}}/d^3 p} \right). \quad (29)$$

In the above equation, $dn_{\text{eq}}/d^3 p$ is the equilibrium distribution and is expressed as Planck's distribution,

$$\frac{dn^{\text{eq}}}{d^3 p} = \frac{2}{(2\pi)^3} \frac{1}{e^{E/T} - 1}. \quad (30)$$

Considering $\tau_{\text{eq}} (= \frac{dn_{\text{eq}}^{\text{eq}}}{d^3 p} / \frac{dR}{d^3 p})$ as the time for equilibration and assuming zero photons at the beginning we can write

$$\frac{dn}{d^3 p} = \frac{dn^{\text{eq}}}{d^3 p} \left(1 - e^{t/\tau_{\text{eq}}} \right). \quad (31)$$

Using the rate equation, the thermalization time can be expressed in a simplified form (considering $E > 2T$) as

$$\tau_{\text{eq}} = \frac{9E}{10\pi\alpha\alpha_s T^2} \frac{1}{\ln(\frac{2.9}{g^2} \frac{E}{T} + 1)}. \quad (32)$$

For energy values $E = 0.5, 1, 2, 3$ GeV, corresponding values for τ_{eq} will be about 270, 356, 505, 639 fm/c, respectively, when the temperature is 200 MeV. As the lifetime of the system is very short, of the order of few tens of fm/c, it is very clear that the high-energy photons will never reach the equilibrium state in heavy-ion collisions. This is an important confirmation for the validity of the assumption made in all such studies that photons, once produced in the collision, leave the system without any further re-interaction.

2.5 Photons from Hot Hadronic Matter

Hot hadronic matter produced after the hadronization of the quark–gluon plasma will also lead to production of photons due to hadronic reactions. These photons will dominate the spectrum at lower p_T (< 1 GeV). The first ever calculation of production of thermal photons from hadronic matter was performed by Kapusta et al. [36, 37].

In a hot hadronic gas (having temperature of the order of pion mass), the most important hadronic constituents for photon production are π and ρ mesons (see Fig. 9). The low mass of pions and the large spin-iso-spin degeneracy of ρ mesons make them the most easily accessible particles in the medium. In order to illustrate the photon production from these two mesons, we closely follow the treatment of KLS [36, 37]. In a hadronic reaction involving charged π and ρ meson, the typical Lagrangian describing the interaction can be written as

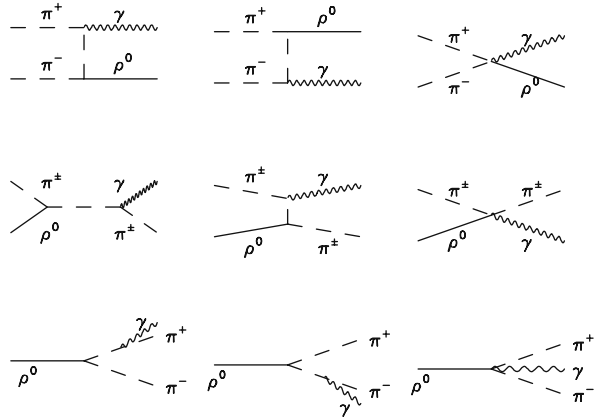


Fig. 9 Typical hadronic reactions for photon production

$$\mathcal{L} = |D_\mu \Phi|^2 - m_\pi^2 |\Phi|^2 - \frac{1}{4} \rho_{\mu\nu} \rho^{\mu\nu} + \frac{1}{2} m_\rho^2 \rho_\mu \rho^\mu - \frac{1}{4} F_{\mu\nu} F^{\mu\nu}, \quad (33)$$

where $D_\mu = \partial_\mu - ieA_\mu - ig_\rho \rho_\mu$, Φ is the complex pion field, $\rho_{\mu\nu}$ is the ρ field strength, and $F_{\mu\nu}$ is the photon field tensor. The differential cross sections for the dominating photon-producing process ($\pi\rho \rightarrow \pi\gamma$) in the hadronic phase are expressed as [36, 37],

$$\begin{aligned} \frac{d\sigma}{dt}(\pi^+ \rho^0 \rightarrow \pi^+ \gamma) &= \frac{d\sigma}{dt}(\pi^- \rho^0 \rightarrow \pi^- \gamma) \\ &= \frac{\alpha g_\rho^2}{12 s p_{\text{c.m.}}^2} \left[2 - \frac{(m_\rho^2 - 4m_\pi^2)s}{(s - m_\pi^2)^2} - (m_\rho^2 - 4m_\pi^2) \right. \\ &\quad \times \left. \left(\frac{s - m_\rho^2 + m_\pi^2}{s - m_\pi^2} \frac{1}{u - m_\pi^2} + \frac{m_\pi^2}{(u - m_\pi^2)^2} \right) \right]. \end{aligned} \quad (34)$$

Similarly for

$$\begin{aligned} \frac{d\sigma}{dt}(\pi^- \rho^+ \rightarrow \pi^0 \gamma) &= \frac{d\sigma}{dt}(\pi^+ \rho^- \rightarrow \pi^0 \gamma) \\ &= -\frac{\alpha g_\rho^2}{48 s p_{\text{c.m.}}^2} \left[4(m_\rho^2 - 4m_\pi^2) \left[\frac{u}{(u - m_\pi^2)^2} + \frac{t}{(t - m_\rho^2)^2} \right. \right. \\ &\quad - \left. \left. \frac{m_\rho^2}{s - m_\pi^2} \left(\frac{1}{u - m_\pi^2} + \frac{1}{t - m_\rho^2} \right) \right] + \left[\left(3 + \frac{s - m_\pi^2}{m_\rho^2} \right) \right. \\ &\quad \times \left. \left. \frac{s - m_\pi^2}{t - m_\rho^2} \right] - \frac{1}{2} + \frac{s}{m_\rho^2} - \left(\frac{s - m_\pi^2}{t - m_\rho^2} \right)^2 \right] \end{aligned} \quad (35)$$

and also

$$\begin{aligned}
 \frac{d\sigma}{dt}(\pi^0\rho^+ \rightarrow \pi^+\gamma) &= \frac{d\sigma}{dt}(\pi^0\rho^- \rightarrow \pi^-\gamma) \\
 &= \frac{\alpha g_\rho^2}{48 s p_{\text{c.m.}}^2} \left[\frac{9}{2} - \frac{s}{m_\rho^2} - \frac{4(m_\rho^2 - 4m_\pi^2)s}{(s - m_\pi^2)^2} \right. \\
 &\quad + \frac{(s - m_\pi^2)^2 - 4m_\rho^2(m_\rho^2 - 4m_\pi^2)}{(t - m_\rho^2)^2} \\
 &\quad + \frac{1}{t - m_\rho^2} \left(5(s - m_\pi^2) - \frac{(s - m_\pi^2)^2}{m_\rho^2} \right. \\
 &\quad \left. \left. - \frac{4(m_\rho^2 - 4m_\pi^2)}{s - m_\pi^2}(s - m_\pi^2 + m_\rho^2) \right) \right]. \quad (36)
 \end{aligned}$$

In the above set of equations, s , t , u are the Mandelstam variables and $p_{\text{c.m.}}$ is the three momentum of the interacting particles in their center-of-mass frame. Typical results are shown in Fig. 10.

Xiong et al. [46] and Song [47] first introduced the $\pi\rho \rightarrow a_1 \rightarrow \pi\gamma$ channel for photon production in hadronic phase, whereas baryonic processes and medium modification were included by Alam et al. [48, 49]. Several refinements, e.g., inclusion of strange sector, use of massive Yang–Mills theory, and t -channel exchange of ω mesons, were incorporated by Turbide et al. [50]. The last calculation is essentially the state-of the-art result at the moment. Photon spectra considering a complete leading rate from QGP [42] and exhaustive reactions in hadronic matter [36, 37, 50] are shown in Fig. 11.

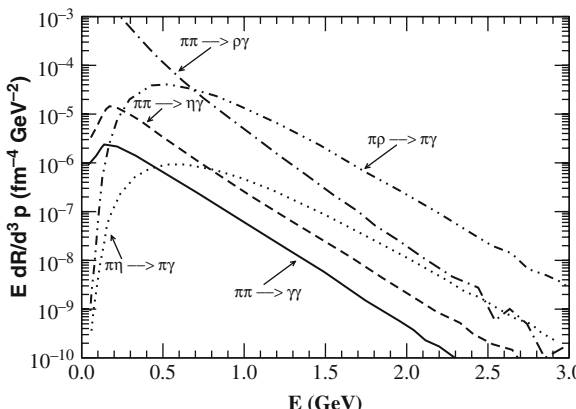


Fig. 10 *Left panel:* Yield of photons from different hadronic channels (taken from [36, 37])

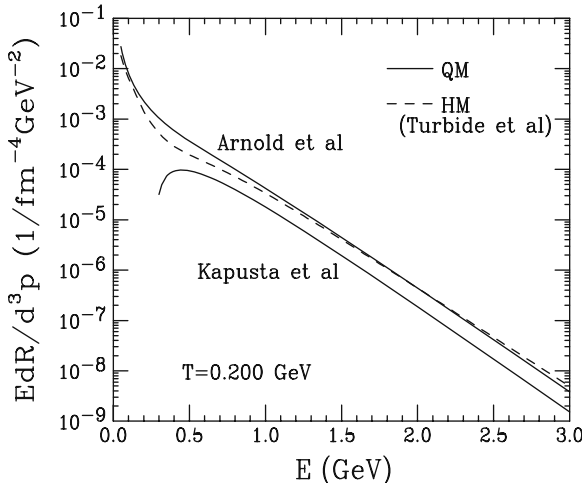


Fig. 11 Complete leading order rates from QGP and exhaustive reactions in hadronic matter [36, 37, 42, 50]

3 Photons from Pb+Pb@SPS to Au+Au@RHIC

3.1 SPS

In order to get an idea of greatly increased insights provided by single photon production, let us briefly recall some of the important results from the SPS era, many of which preceded the large strides made in our theoretical understanding mentioned above. The first hint of single photon production, which later turned out to be the upper limit of their production, came from the $S + \text{Au}$ collisions studied at the SPS energies [51].

These results were analyzed in two different scenarios by authors of [52]. In the first scenario, a thermally and chemically equilibrated quark-gluon plasma was assumed to be formed at some initial time ($\tau_0 \approx 1 \text{ fm}/c$), which expanded [53], cooled, and converted into a mixed phase of hadrons and QGP at a phase-transition temperature, $T_C \approx 160 \text{ MeV}$. When all the quark matter was converted into a hadronic matter, the hot hadronic gas continued to cool and expand, and underwent a freeze-out at a temperature of about 140 MeV. The hadronic gas was assumed to consist of π , ρ , ω , and η mesons, again in thermal and chemical equilibrium. This was motivated by the fact that the included hadronic reactions involved [36, 37] these mesons. This was already a considerable improvement over a gas of massless pions used in the literature at that time. In the second scenario, the collision was assumed to lead to a hot hadronic gas of the same composition. The initial temperature was determined by demanding that the entropy of the system be determined from the measured particle rapidity density [54]. It was found that the scenario which did not involve a formation of QGP led to a much larger initial temperature and a production of photons which was considerably larger than the upper limit of

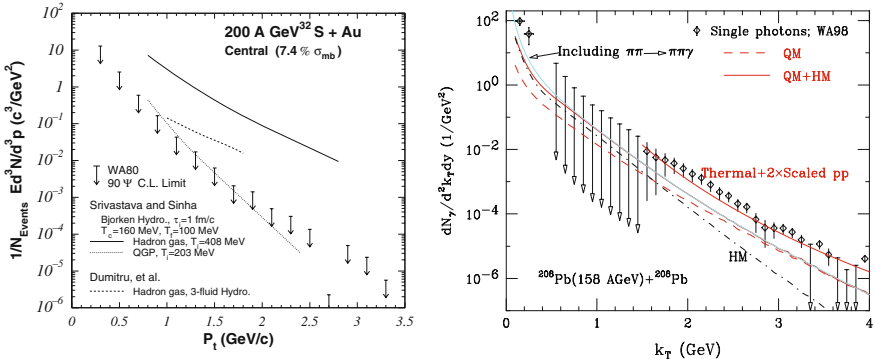


Fig. 12 *Left panel:* Upper limits at the 90% confidence level on the invariant excess photon yield for the 7.4% σ_{mb} most central collisions of 200A GeV $^{32}\text{S} + \text{Au}$ [51]. The solid and the dashed curves give the thermal photon production expected from hot hadron gas calculation [52], while the dotted curve is the calculated thermal photon production expected in the case of a QGP formation. *Right panel:* Single photon production in $\text{Pb}+\text{Pb}$ collision at CERN SPS. Prompt photons are estimated using pQCD (with a K -factor estimated using NLO calculation) and intrinsic k_T of partons [55]

the photon production, and could be ruled out. The calculation assuming a quark–hadron phase transition yielded results which were consistent with the upper limit of the photon production. These results were confirmed [56–62] by several calculations exploring different models of expansion (see left panel of Fig. 12).

It was soon realized that one may not limit the hadronic gas to contain just π , ρ , ω , and η mesons, as there was increasing evidence that perhaps all the mesons and baryons were being produced in a thermal and chemical equilibrium in such collisions. Thus authors of [63] explored the consequences of using a hadronic gas consisting of essentially all the hadrons in the Particle Data Book, in a thermal and chemical equilibrium. This led to an interesting result for the $\text{Pb}+\text{Pb}$ collision at SPS energies, for which experiments were in progress. It was found that with the rich hadronic gas, the results for the production of photons in the phase-transition and no-phase-transition models discussed above were quite similar, suggesting that measurement of photons at the SPS energy could perhaps not distinguish between the two cases. However, in a very important observation, it was also noted that the calculations involving hot hadronic gas at the initial time would lead to hadronic densities of several hadrons/fm³, and while those involving a quark–gluon plasma in the initial state would be free from this malady. Thus, it was concluded that the calculations involving a phase transition to QGP offered a more natural description.

The WA98 experiment [15] reported the first observation of direct photons in central 158A GeV $\text{Pb}+\text{Pb}$ collisions studied at the CERN SPS. This was explained [64] in terms of formation of quark–gluon plasma in the initial state (at $\tau_0 \approx 0.2$ fm/c), which expanded, cooled, and hadronized as in [63] (see right panel of Fig. 12). An independent confirmation of this approach was provided by an accurate

description [65] of excess dilepton spectrum measured by the NA60 experiment for the same system.

Once again the results for single photons were analyzed by several authors using varying models of expansion as well as rates for production of photons; viz., with or without medium modification of hadronic properties (see, e.g., [50, 66–69]). The outcome of all these efforts can be summarized as follows: the single photon production in Pb+Pb collisions at SPS energies can be described either by assuming a formation of QGP in the initial state or by assuming the formation of a hot hadronic gas whose constituents have massively modified properties. The later description, however, involved a hadronic density of several hadrons/fm³, which raises doubts about the applicability of a description in terms of hadrons, as suggested by [63].

3.2 RHIC

The first experimental photon result obtained from the relativistic heavy-ion collider was the centrality dependent single photon data for 200A GeV Au+Au collisions by PHENIX collaboration [16], where single photons were identified clearly for $p_T > 4$ GeV. For central collisions, the lower bound on photon transverse momenta was even much lower, upto 2 GeV (Fig. 13). Those data were in good agreement with NLO pQCD results for pp collisions, scaled by number of binary collisions (without considering the iso-spin effect).

Thermal radiation dominates the direct photon spectrum at lower values of p_T (≤ 3 GeV) and the measured slope of the thermal photon spectrum can be related to the temperature of the system.

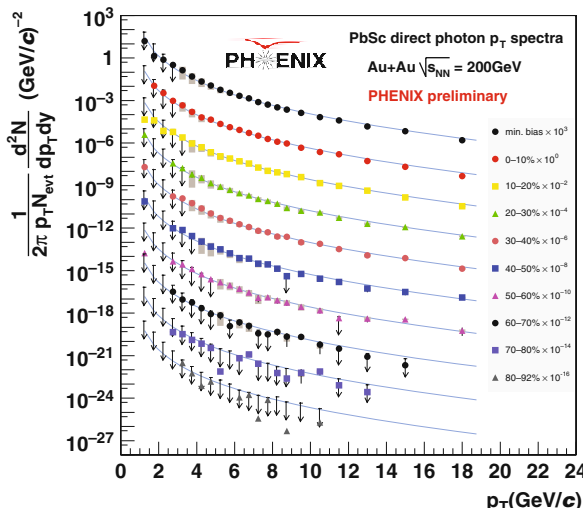


Fig. 13 Direct photon results for Au+Au collisions (left panel) and $p + p$ collisions (right panel) at $\sqrt{s_{NN}} = 200A$ GeV [16]

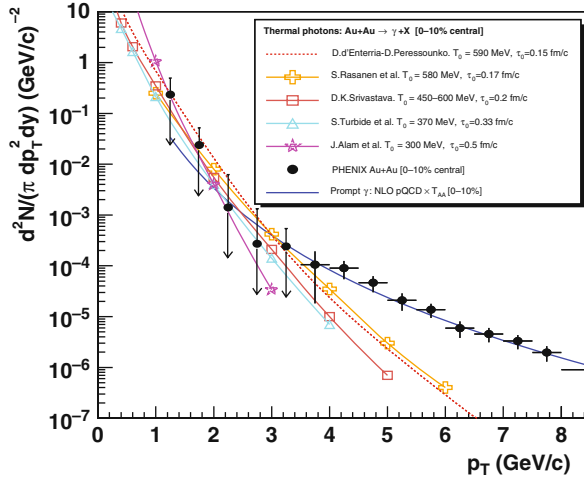


Fig. 14 Thermal photon spectra for central 200A GeV Au+Au collision computed within different models [71] compared to the expected pQCD prompt photon yield and to the experimental total direct photon spectrum measured by PHENIX [32]

In Fig. 14 results from several theoretical models based on hydrodynamics for thermal photon production at RHIC are shown. The initial temperature and thermalization time for Au+Au collision at 200A GeV quoted by several theoretical groups [50, 64, 66–71] are in the range of 450–650 MeV and about 0.2 fm/c, respectively.

All these calculations are comparable to the experimental data and with each others within a factor of 2 and also confirm the dominance of thermal radiation in the direct photon spectrum in low and intermediate p_T range.

3.2.1 Indications for Jet Conversion Photons

We have already discussed the procedure for calculating the high-energy photons due to passage of jets through the quark–gluon plasma.

The parametrized p_T distribution of jets (quarks, antiquarks, and gluons) obtained by using CTEQ5L parton distribution function and EKS98 nuclear modification factor is given by

$$\frac{dN_{\text{jet}}}{dp_T dy} \Big|_{y=0} = T_{AA} \frac{d\sigma_{\text{jet}}}{d^2 p_T dy} \Big|_{y=0} = K \frac{a}{(1 + p_T/b)^c}. \quad (37)$$

Here, $T_{AA} = 9A^2/8\pi R_{\perp}^2$ is the nuclear thickness for a head-on collision and to include the higher order effects a K -factor of 2.5 is introduced. Numerical values for the parameters for quarks, antiquarks, and gluons can be found in [13].

Now as a first step, let us ignore the transverse expansion of the plasma and assume that a thermally and chemically equilibrated plasma is produced in the collision at an initial time τ_0 at temperature T_0 . In an isentropic longitudinal expansion,

T_0 and τ_0 are related by the observed particle rapidity density (dN/dy) by

$$T_0^3 \tau_0 = \frac{2\pi^4}{45\zeta(3)} \frac{1}{4a\pi R_\perp^2} \frac{dN}{dy}, \quad (38)$$

where $a = 42.25\pi^2/90$, for QGP consisting of u , d , and s quarks and gluons. dN/dy can be taken as $\simeq 1260$, based on the charge particle pseudorapidity density measured by PHOBOS experiment [72] for central collision of Au nuclei at $\sqrt{s_{NN}} = 200$ GeV. For central collision of Pb nuclei at LHC energies $dN/dy \simeq 5625$ was used by Fries et al. [13] as in [73].

Further assuming a rapid thermalization, initial conditions can then be estimated as [73] $T_0 = 446$ MeV and $\tau_0 = 0.147$ fm/c for the RHIC and $T_0 = 897$ MeV and $\tau_0 = 0.073$ fm/c for the LHC. Now, taking the nuclei to be uniform spheres, the transverse profile for initial temperature is given by $T(r) = T_0[2(1 - r^2/R_\perp^2)]^{1/4}$, where $R_\perp = 1.2A^{1/3}$ fm. The same profile $R(r) = 2(1 - r^2/R_\perp^2)$ is used for the jet production.

The jet traverses the QGP medium until it reaches the surface or until the temperature drops to the transition temperature T_c (~ 160 MeV).

First estimates for the jet conversion photons at RHIC and LHC energies along with other sources of photons having large transverse momentum are given in Fig. 15. We see that the jet conversion photons make a fairly large contribution in the p_T range of 4–10 GeV.

The centrality dependence of jet conversion photons was also studied by Fries et al. [74] (see Fig. 16), which indicates a small but clear contribution of photons due to passages of jets through the plasma. These early calculations have been brought to a high degree of sophistication by the McGill group [75] (see Fig. 17), where jet quenching and jet-photon conversion along with bremsstrahlung is treated in a single framework. The details can be seen in [75].

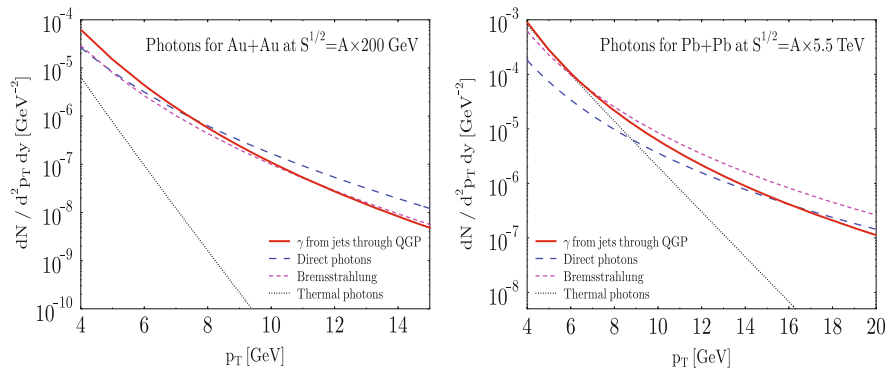


Fig. 15 Jet conversion photons at RHIC [left panel] and LHC [right panel] energies (taken from [13])

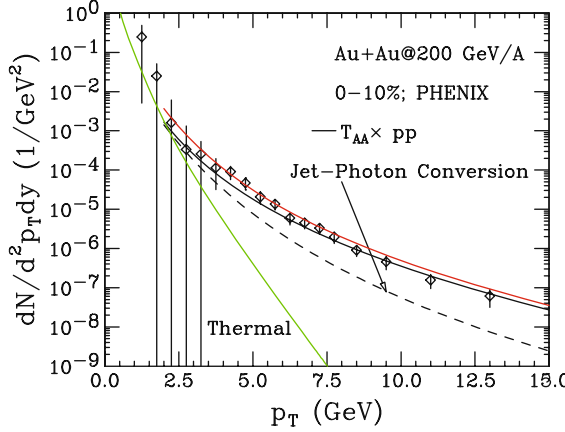


Fig. 16 Photon yield as a function of p_T in central (0–10%) Au+Au collisions at 200A GeV. Results of jet-photon conversion (solid and labeled), primary hard photons (dashed), and the sum of the two (upper-most solid curve) along with thermal photons are shown separately. Data are from the PHENIX collaboration [32]

In Fig. 17, the results for thermal photons, direct photons due to primary processes, bremsstrahlung photons, and the photons coming from jets passing through the QGP in central collision of gold nuclei at RHIC energies are plotted. The quark jets passing through the QGP give rise to a large yield of high-energy photons. For RHIC this contribution is a dominant source of photons up to $p_T \simeq 6$ GeV. Due to multiple scattering suffered by the fragmenting partons a suppression of the bremsstrahlung contribution is found. This will further enhance the importance of the jet-photon conversion process.

Obviously a high statistics data at several centralities and energies will go a long way in clearly establishing the presence of jet conversion photons at RHIC and

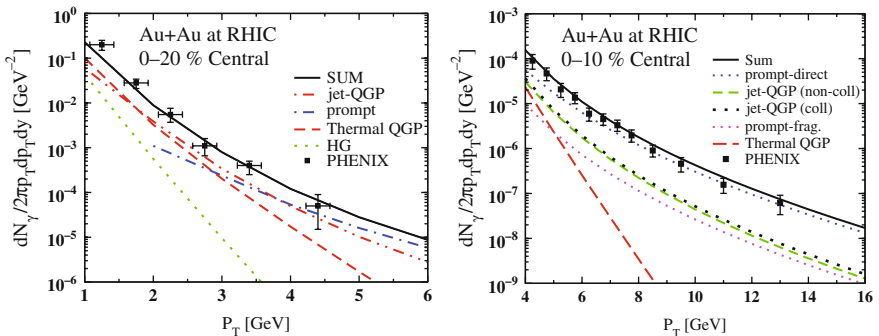


Fig. 17 Yield of photons in Au+Au collisions at RHIC, for centrality classes 0–10% (left panel) and 0–10% (right panel). See [75] for details. The data sets are from [76] and [32], respectively

LHC energies. This is also of importance, as there are indications that these photons measure the initial spatial anisotropy of the system [75].

4 Dileptons

Virtual photons or dileptons are also very powerful and efficient probes like the real photons to study the dynamics of heavy-ion collisions and the properties of the medium created in the collisions. Real photons are massless, whereas dileptons are massive. Thus, invariant mass M and the transverse momentum p_T are the two parameters available for dileptons, which can be tuned to investigate the different stages of the expanding fireball. Dileptons having large invariant mass and high p_T are emitted very early, soon after the collision when the temperature of the system is very high. On the other hand, those having lower invariant masses come out later from a relatively cooler stages and at low temperatures.

Similar to the real photons, dileptons are also emitted from every stage of heavy-ion collisions [2]. In the QGP phase, a quark can interact with an antiquark to form a virtual photon γ^* , which subsequently decays into a lepton (l^-) and an anti-lepton (l^+) pair, together known as dilepton. In the hadronic phase, dileptons are produced from interactions of charged hadrons with their anti-particles by processes like $(\pi^+ + \pi^- \rightarrow l^+ + l^-)$ (see Fig. 18). They are also produced from decay of hadronic resonances like ρ , ω , ϕ , and J/Ψ as well as from Drell–Yan process. In the Drell–Yan process, a valence quark from a nucleon in the projectile nucleus interacts with a sea antiquark from a nucleon in the target nucleus to form a virtual photon, which decays into a lepton pair. The dilepton emissions can be classified into three distinct regimes in a rough estimation, depending on the invariant mass M of the emitted lepton pairs. These are

- (a) Low mass region (LMR): $M \leq M_\phi (= 1.024 \text{ GeV})$: In this mass range, vector meson decays are the dominating source of dilepton production and medium-modified spectral density is one of the key issues which needs to be addressed.

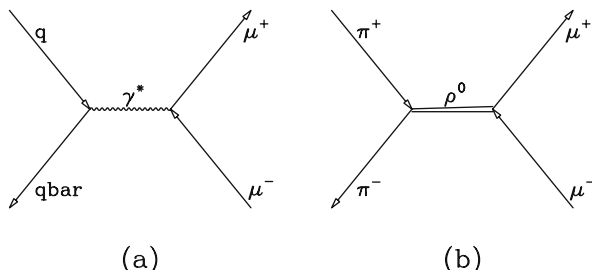


Fig. 18 Dilepton production from (a) quark–antiquark annihilation and (b) $\pi^+\pi^-$ annihilation through ρ channel

- (b) Intermediate mass region (IMR): $M_\phi < M < M_{J/\psi} (= 3.1 \text{ GeV})$: In intermediate mass region, continuum radiation from QGP dominates the dilepton mass spectrum and thus this region is important for getting a pure QGP signature.
- (c) High mass region (HMR): $M \geq M_{J/\psi}$: In the HMR, the most interesting phenomenon is the primordial emission and heavy quarkonia like J/Ψ and Υ suppression.

A schematic diagram of continuous dilepton mass spectrum is shown in Fig. 19.

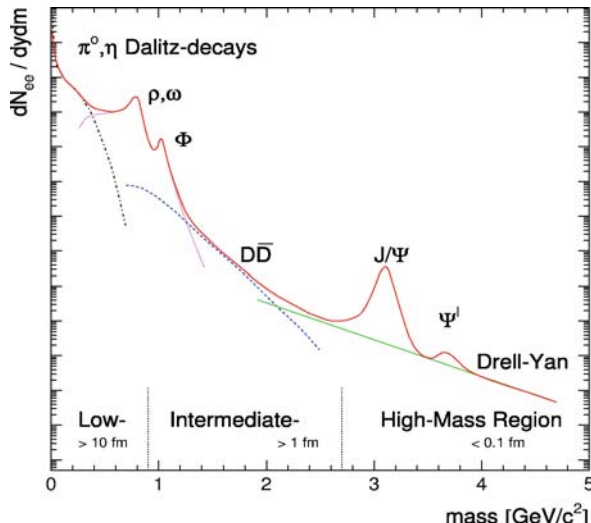


Fig. 19 Expected sources of dilepton production as a function of invariant mass in relativistic heavy-ion collisions (schematic)

4.1 Dileptons from QGP and Hadronic Phase

Dilepton production by quark–antiquark annihilation process or by $\pi^+ \pi^-$ annihilation process can be expressed in a general form as

$$a^+ + a^- \rightarrow l^+ + l^- \quad (39)$$

where the particle “ a ” can be either a quark or a π meson. We closely follow the treatment of [14] for calculation of dilepton spectra in this section. From quantum electrodynamics (QED), the cross section for $e^+e^- \rightarrow \mu^+\mu^-$ can be written as

$$\tilde{\sigma}(M) = \frac{4\pi}{3} \frac{\alpha^2}{M^2} \left[1 + \frac{2m_l^2}{M^2} \right] \left[1 - \frac{4m_l^2}{M^2} \right]^{1/2}. \quad (40)$$

In the above equation, α is the fine structure constant ($\approx 1/137$), m_l is the mass of μ , and M is the dilepton-invariant mass. For the quark–antiquark annihilation process, this cross section is modified by inclusion of a color factor $N_c (= 3)$ and the fractional charges of the up(u) and down(d) quarks. Thus, the new cross section takes the form as

$$\sigma_q(M) = F_q \tilde{\sigma}(M), \quad (41)$$

$$F_q = N_c (2s + 1)^2 \sum_f e_f^2, \quad (42)$$

where s is the spin of quarks, e_f is the fractional charge, and the sum is over different quark flavor “ f . ” If we consider only u and d quarks having fractional charges $1/3$ and $2/3$, respectively, then the factor F_q is $20/3$.

In the hadronic phase, the $\pi^+ \pi^-$ annihilation from vector meson dominance model can be expressed as

$$\pi^+ + \pi^- \rightarrow \rho \rightarrow l^+ + l^-. \quad (43)$$

For this case, the QED cross section is multiplied by form factor $F_\pi(M)$ which is of Breit–Wigner form as

$$F_\pi(M) = \frac{m_\rho^4}{(m_\rho^2 - M^2)^2 + m_\rho^2 \Gamma_\rho^2}. \quad (44)$$

Here, M_ρ is the mass of the ρ meson (~ 770 MeV) and Γ_ρ (~ 155 MeV) is the decay width. Thus, the total pion cross section as a function of M becomes

$$\sigma_\pi(M) = F_\pi \tilde{\sigma}(M) (1 - 4m_\pi^2/M^2)^{1/2}. \quad (45)$$

The reaction rate “ R ” can be obtained from the kinetic theory:

$$R(a^+ a^- \rightarrow l^+ l^-) = \int \frac{d^3 p_1}{(2\pi)^3} f(\mathbf{p}_1) \int \frac{d^3 p_2}{(2\pi)^3} f(\mathbf{p}_2) \sigma(a^+ a^- \rightarrow l^+ l^-; \mathbf{p}_1 \mathbf{p}_2) v_{rel} \quad (46)$$

where

$$v_{rel} = \frac{[(p_1 \cdot p_2)^2 - m_a^4]^{1/2}}{E_1 E_2}, \quad (47)$$

$f(\mathbf{p})$ is the occupation probability at momentum \mathbf{p} , and energy $E = \sqrt{\mathbf{p}^2 + m_a^2}$. Now, using the distribution function $f(\mathbf{p}) \sim e^{-E/T}$ and integrating over five out of the six variables, the reaction rate takes a simplified form as

$$R(T) = \frac{T^6}{(2\pi)^4} \int_{z_0}^{\infty} \sigma(z) z^2 (z^2 - 4z_a^2) K_1(z) dz. \quad (48)$$

Here, $z = M/T$, $z_a = m_a/T$, and K_1 is the modified Bessel function of the first kind. The value of the parameter z_0 is taken as the larger of $2m_a/T$ and $2m_l/T$. Now, for massless u and d quarks (as $m_u, m_d \ll T$), the e^+e^- emission rate takes a simple form of T^4 law,

$$R = \frac{10}{9\pi^3} \alpha^2 T^4. \quad (49)$$

One can also estimate the relaxation time for lepton pairs to come to equilibrium with the QGP:

$$t_{\text{rel}} = \frac{n_{\text{eq}}^l}{2R} = \frac{9\pi}{10\alpha^2 T}. \quad (50)$$

For a temperature range of 200–500 MeV, the value of t_{rel} varies from 20 to 60×10^3 fm/c. We know that the lifetime of the QGP phase is only ~ 10 fm/c, which is more than three order of magnitude smaller than t_{rel} . Thus, like the real photons, the produced lepton pairs also escape the system without suffering significant absorption in the medium.

Now, the dilepton emission rate R is actually defined as the total number of lepton pairs emitted from a 4-volume element d^4x ($= d^2x_T d\eta \tau d\tau$) at a particular temperature T is given by

$$R = dN/d^4x. \quad (51)$$

Thus, the rate of production of dileptons having invariant mass M can be expressed using Eq. (46) as

$$\frac{dN}{d^4x dM^2} = \frac{\sigma(M)}{2(2\pi)^4} M^3 T K_1(M/T) \left[1 - \frac{4m_a^2}{M^2} \right]. \quad (52)$$

From the last equation and using properties of the modified Bessel's functions, the production rate per unit 4-volume for total energy E , momentum p , and invariant mass M (where $E = \sqrt{p^2 + M^2}$) can be written as

$$E \frac{dN}{d^4x dM^2 d^3p} = \frac{\sigma(M)}{4(2\pi)^5} M^2 e^{-E/T} \left[1 - \frac{4m_a^2}{M^2} \right]. \quad (53)$$

Integrating the rate of emission over the entire 4-volume from QGP and hadronic phase, one can obtain the p_T spectra at a particular M as

$$\frac{dN}{dM^2 d^2 p_T dy} = \int \tau d\tau r dr d\eta d\phi \left[\left[E \frac{dR}{dM^2 d^3 p} \right]_{\text{QGP}} f_{\text{QGP}}(r, \tau) + \left[E \frac{dR}{dM^2 d^3 p} \right]_{\text{HM}} f_{\text{HM}}(r, \tau) \right], \quad (54)$$

where η is the space–time rapidity. In the above equation, the temperature T , QGP, and hadronic matter (HM) distribution functions (f_{QGP} , f_{HM}) all are functions of space $\mathbf{r}(x, y)$, transverse velocity v_T , and proper time τ . Equation (54) can be solved numerically by using any appropriate model [e.g., [77]] with a proper equation of state (EOS). One can also get the invariant mass spectrum by integrating out the variable p_T from Eq. (54). The invariant mass spectrum of thermal dilepton is dominated by QGP radiation above ϕ mass and hadronic radiation outshines the QGP contribution for $M \leq M_\phi$.

4.2 Medium Modification

As mentioned earlier, in the low-mass region, dilepton emission is largely mediated by $\rho(770)$, a broad vector meson, as a result of its strong coupling to the $\pi\pi$ channel and a short lifetime, which is about $1.3 \text{ fm}/c$. In-medium properties of vector mesons, like change in medium mass and width, have long been considered as prime signatures of a hot and dense hadronic medium. CERES/NA45 [78, 79] started the pioneering experiment on dilepton measurement during the period 1989–1992 at CERN SPS. For $p + \text{Be}$ and $p + \text{Au}$ collisions, the theoretical estimates, considering only hadron decay (as source of dilepton production), were in excellent agreement with the experimental data points. However, the CERES/NA45 experimental data for $S + \text{Au}$ and $\text{Pb} + \text{Au}$ at $200A \text{ GeV}$ and $158A \text{ GeV}$, respectively, exhibit excess radiation beyond the electromagnetic final state decay of produced hadrons below the ϕ mass. From these observations, it was concluded that the theoretical models based on $\pi\pi$ annihilation can reproduce the experimental data, only if the properties of the intermediate ρ meson are modified in the medium. This was an exciting discovery and a genuine consequence of many-body physics. However, the resolution and statistical accuracy of the data were insufficient to distinguish between models suggesting a drop in the mass of ρ mesons [80] and those which suggest an increase in their decay width [81] and thus, determine the in-medium spectral properties of the ρ meson.

Shortly after this, an excess dimuon (over the sources expected from pA measurement) was identified experimentally by Helios/3 [82, 83] (measured both e^+e^- and $\mu^+\mu^-$) and NA38/NA50 [84] collaborations.

Rapp and Shuryak [85] and Kvasnikova et al. [65] showed that the excess dimuon observed by NA50 in the mass region $1.5 < M < 2.5 \text{ GeV}$ can be explained by thermal signal without invoking any anomalous enhancement in the charm production. Kvasnikova et al. studied the NA50 intermediate mass dimuon result using hydrodynamic model and a detailed analysis of the rates of dilepton production from

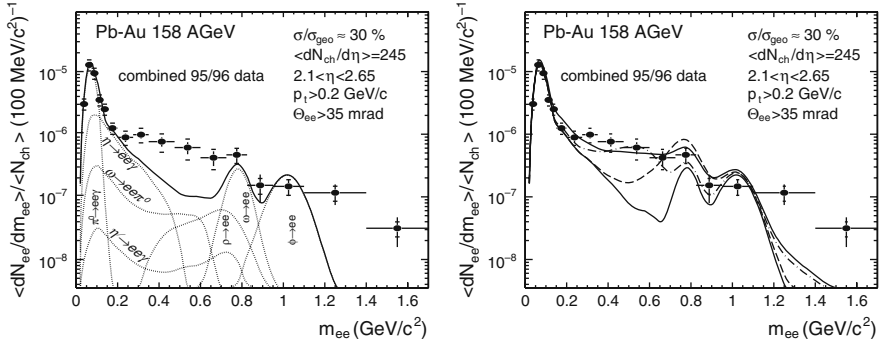


Fig. 20 *Left panel:* Invariant mass spectrum of e^+e^- pairs emitted in 158A GeV Pb + Au collisions from the combined analysis of 1995 and 1996 data by CERES/NA45 [78, 79]. The *solid line* shows expected yield from hadron decay and *dashed lines* indicate the individual contribution to the total yield. *Right panel:* Comparison of the experimental data to (i) free hadron decays without ρ decays (*thin solid line*), (ii) model calculations with a vacuum ρ spectral function (*thick dashed line*), (iii) with dropping in-medium ρ mass (*thick dash-dotted line*), and (iv) with a medium-modified ρ spectral function (*thick solid line*)

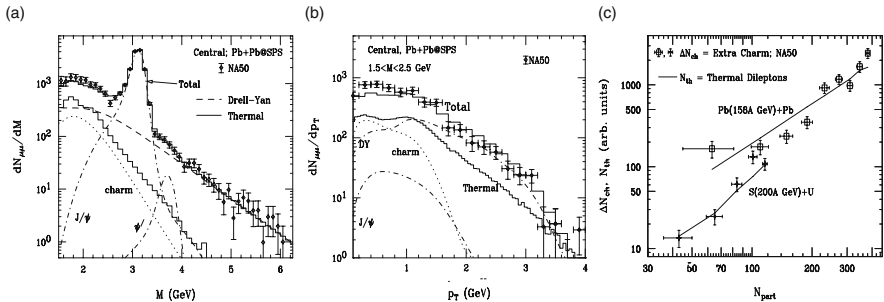


Fig. 21 (a) The dimuon invariant mass spectrum after correcting for detector acceptance and resolution and NA50 data. The Drell-Yan and thermal contributions are shown separately along with correlated charm decay and direct decays of the J/Ψ and \bar{J}/Ψ . (b) The dimuon transverse momentum spectrum. (c) Centrality dependent results from [65] and NA50 data [84]

hadronic phase [65]. Detector resolution and acceptance were accurately modeled in their calculation and the normalization was determined by a fit to the Drell-Yan data using the MRSA parton distribution function as done in the experimental NA50 analysis. The results are shown in Fig. 21. They also studied the centrality dependence of the NA50 data using hydrodynamics by incorporating azimuthal anisotropy in the calculation. The results were in fairly good agreement with the measured excess dilepton data, as can be seen in the third panel of Fig. 21.

4.2.1 Dropping m_ρ vs. Increasing Γ_ρ

The CERES data were unable to distinguish between the models suggesting drop in the mass of ρ meson and those suggesting an increase in its width, as seen in Fig. 20.

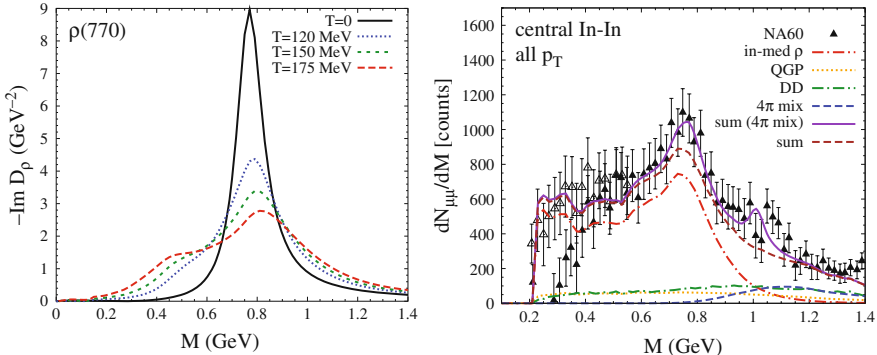


Fig. 22 *Left panel:* In-medium vector meson spectral functions from hadronic many-body theory. The ρ in cold nuclear matter at several densities proportional to the saturation density $\rho_0 = 0.16 \text{ fm}^{-3}$. *Right panel:* NA60 [86] excess dimuons in central In + In collisions at SPS compared to thermal dimuon radiation using in-medium electromagnetic rates [87]

The high statistics data obtained by the NA60 Collaboration for In + In collisions at SPS energies for the dimuon excess rather clearly ruled out the models advocating the dropping mass scenarios. They rather firmly establish the models advocating the substantial broadening of the decay width of the ρ meson due to many-body effects (see Fig. 22).

5 Elliptic Flow

Elliptic flow is one of the key observables in relativistic collisions of heavy nuclei, which confirms the collectivity and early thermalization in the created hot and dense matter. For a non-central collision (impact parameter $b \neq 0$) of two spherical nuclei, the overlapping zone between the nuclei no longer remains circular in shape, rather it takes an almond shape. This initial spatial anisotropy of the overlapping zone is converted into momentum space anisotropy of particle distribution via the action of azimuthally anisotropic pressure gradient, which gives rise to elliptic flow [88]. Note that, this anisotropic flow or elliptic flow can also be produced in central collisions of deformed nuclei, such as U + U collisions [89]. The driving force for momentum anisotropy is the initial spatial eccentricity $\epsilon_x (= \langle y^2 - x^2 \rangle / \langle y^2 + x^2 \rangle)$ and the momentum anisotropy can grow as long as $\epsilon_x > 0$ [90]. Elliptic flow coefficient v_2 is quantified as the second Fourier coefficient of particle distribution in the p_T space, which is of the form:

$$\frac{dN(b)}{p_T dp_T dy d\phi} = \frac{dN(b)}{2\pi p_T dp_T dy} (b) \times [1 + 2v_1(p_T, b) \cos(\phi) + 2v_2(p_T, b) \cos(2\phi) + 2v_3(p_T, b) \cos(3\phi) + \dots]. \quad (55)$$

At midrapidity ($y = 0$) and for collisions of identical nuclei, only the even cosine terms survive in the above Fourier series and v_2 is the lowest non-vanishing anisotropic flow coefficient. Now, the value of v_2 depends on the impact parameter b , transverse momentum p_T , as well as on the particle species through their rest masses m . For massless real photons, v_2 depends on the elliptic flow of parent particles.

5.1 Thermal Photon v_2

Elliptic flow coefficient v_2 for photons is a much more powerful tool than the v_2 of hadrons to study the evolution history of the system depending on the different emission time and production mechanism of photons compared to hadrons. Photons are emitted from all stages and throughout the evolution of the system, whereas hadrons are emitted only from the freeze-out surface at a relatively much cooler temperature (~ 100 MeV). The interplay of the photon contributions from fluid elements at different temperatures with varying radial flow pattern gives the photon v_2 a richness, which is not possible for hadrons. Also, photons emitted from QGP phase as a result of $q\bar{q}$ annihilation and quark-gluon Compton scattering carry the momenta of the parent quarks or antiquarks, which makes them an unique tool for QGP study.

Ideal hydrodynamic model has successfully predicted the elliptic flow for different hadronic species upto a p_T value of 1.5(2.3) GeV for mesons (baryons) [90] at RHIC. Experimental data show that $v_2(p_T)$ for hadrons saturate beyond that p_T range. However, ideal hydrodynamics predicted $v_2(p_T)$ rises monotonically with p_T . The saturation at higher p_T is often explained as due to viscosity, neglected in the discussion here.

Figure 23 shows the p_T -dependent v_2 for thermal photons [10, 11] for a typical impact parameter $b = 7$ fm. Contributions from quark matter (QM) and hadronic matter (HM) along with the sum of the two are shown separately (left panel of

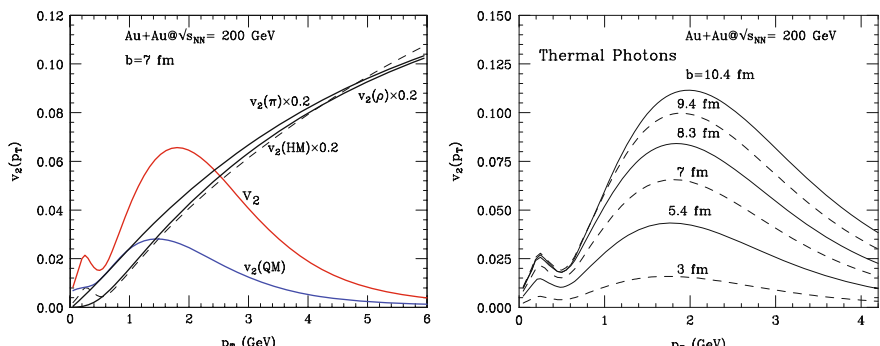


Fig. 23 Left panel: $v_2(p_T)$ for thermal photons along with the v_2 for π and ρ mesons. Contributions from the quark matter and the hadronic matter are shown separately with the sum contribution. Right panel: Thermal photon v_2 for different centrality bins (taken from [10, 11]).

Fig. 23). One can see that $v_2(HM)$ rises monotonically with p_T , similar to the hadronic v_2 predicted by hydrodynamics. On the other hand, $v_2(QM)$ is very small at high p_T or early times, as very little flow is generated by that time. $v_2(QM)$ rises for smaller values of p_T and after attaining a peak value around 1.5–2.0 GeV, it tends to 0 as $p_T \rightarrow 0$. The total flow or $v_2(QM+HM)$ tracks the $v_2(QM)$ at high p_T in spite of very large $v_2(HM)$, as the yield of photons from hadronic phase is very small at high p_T . It is well known and mentioned earlier that, for photon energy larger than the rest masses of the photon-emitting particles, the photon production cross section peaks when the photon momentum and momentum of photon-emitting particles become almost identical [2]. Thus, at high p_T photon v_2 reflects the anisotropies of the quarks and antiquarks at early times. Also, the collision-induced conversion of vector mesons (ρ) starts dominating the photon production for $p_T \geq 0.4$ GeV, which gives rise to a structure at the transition point in the photon v_2 curve [10, 11]. As HM contribution dominates the p_T spectrum and hydrodynamics is well applicable around that p_T range, the structure is expected to survive in the experimental result also.

Recently Turbide et al. [75] have shown that total contribution to photon v_2 from prompt fragmentation (small +ve v_2) and jet-conversion (small -ve v_2) photons is very small, almost equal to zero. Also, we know that the prompt photons from Compton and annihilation processes do not contribute to elliptic flow as their emission is not subjected to collectivity and has azimuthal symmetry. Thus, at low and intermediate p_T range, v_2 from thermal photons plays a dominant role in deciding the nature of the direct photon v_2 .

For central collision of two spherical nuclei, the spatial eccentricity (ϵ) of the overlapping zone is zero, thus the flow coefficient v_2 is also zero. The $v_2(p_T)$ for thermal photons for different centrality bins are shown in the right panel of Fig. 23, where the value of v_2 rises from central toward peripheral collisions. Now, the elliptic flow as well as spatial eccentricity both rise with higher values of impact parameter. However, the ratio of the two remains independent of impact parameter

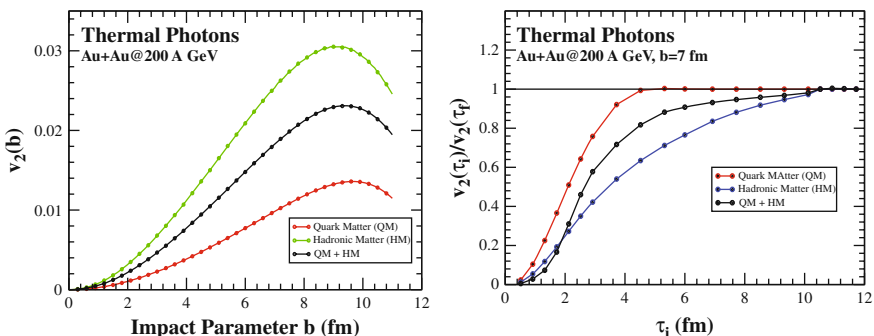


Fig. 24 Left panel: p_T integrated elliptic flow of thermal photons from different phases at RHIC. Right panel: Time evolution of elliptic flow from different phases, normalized by the final value at the time of freeze-out (taken from [91, 92])

up to a very large value of b [91, 92]. The p_T integrated v_2 for thermal photons from different phases as a function of collision centrality shows an interesting behavior (left panel of Fig. 24). The $v_2(b)$ rises with b until for very peripheral collisions. For these, the system size itself becomes very small to generate enough pressure gradient and elliptic flow, and as a result $v_2(b)$ decreases. The p_T -dependent as well as p_T -integrated time evolution results [91, 92] of thermal photon spectra and elliptic flow show explicitly the gradual buildup of spectra and v_2 with time very well. The photon v_2 from QGP phase saturates within about 4–5 fm/c (right panel of Fig. 24), whereas v_2 from hadronic phase is not very significant at early times and it saturates much later.

5.2 Thermal Dilepton v_2

Elliptic flow of thermal dileptons is another very interesting and illustrative observable which gives information of the different stages of heavy ion collision depending on invariant mass M and transverse momentum p_T [93]. At the ρ and ϕ masses, the p_T spectra and $v_2(p_T)$ show complete dominance of hadronic phase. At these resonance masses, radiation from quark matter becomes significant only for very large $p_T (\geq 4)$ GeV (left panel of Fig. 25). The $v_2(p_T)$ at $M = m_\rho$ also shows similar nature as spectra and the total v_2 is almost similar to hadronic v_2 upto a large p_T . Right panel of Fig. 25 shows dilepton v_2 at ρ mass along with v_2 of ρ meson where $v_2(HM)$ tracks $v_2(\rho)$. Also, the hadronic v_2 is little smaller than the $v_2(HM)$ for dileptons. The effective temperature of dilepton emission is a little larger than for hadrons, thus the spectra of the later are boosted by a somewhat larger radial flow [93], which results in smaller elliptic flow.

A totally different situation emerges for the p_T spectrum and v_2 for dilepton invariant mass $M > M_\phi$. For $M = 2$ GeV, the dilepton v_2 is similar to $v_2(QM)$ in spite of the 20 times larger $v_2(HM)$, as hadronic dileptons are very few compared to QGP radiation at this M value (Fig. 26).

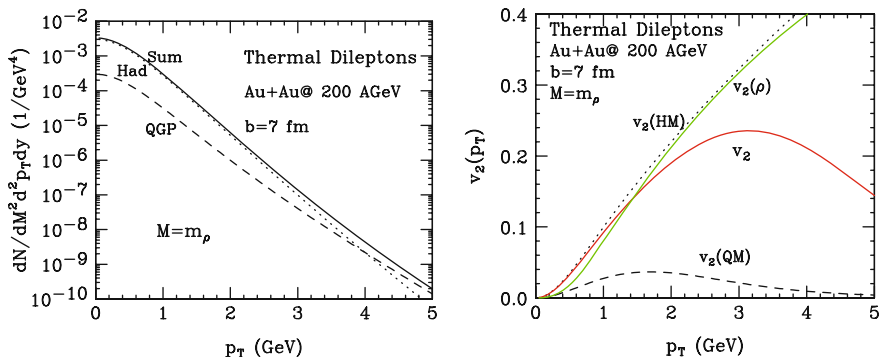


Fig. 25 p_T spectra (left panel) and v_2 (right panel) for thermal dileptons at $M = m_\rho$. $v_2(\rho)$ is also plotted in the v_2 curve for comparison [93]

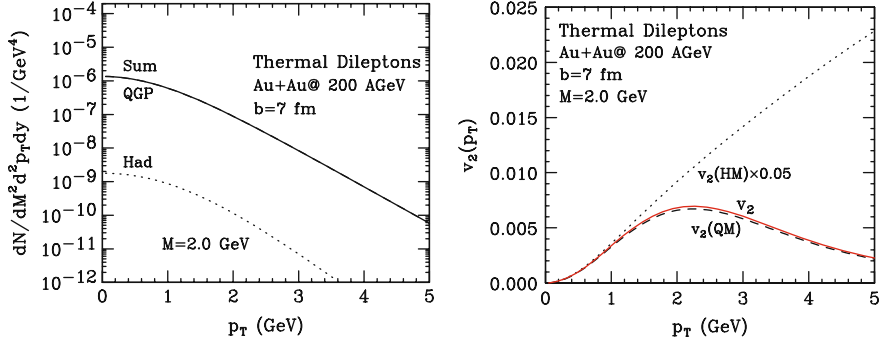


Fig. 26 p_T spectra (left panel) and v_2 (right panel) for thermal dileptons at $M = 2 \text{ GeV}$ [93]

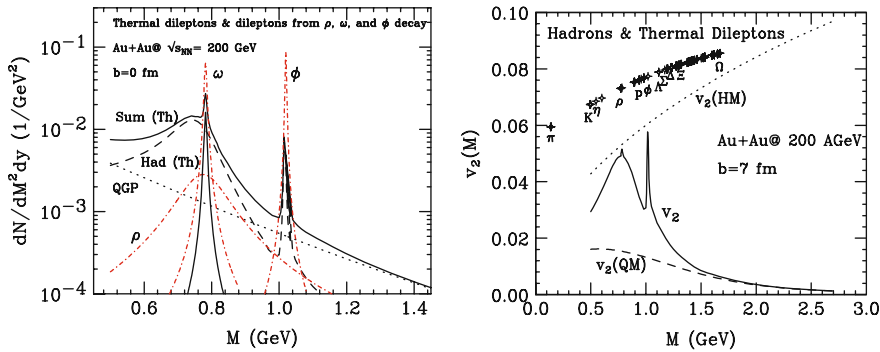


Fig. 27 Left panel: The mass spectra of thermal dileptons from a hydrodynamical simulation of central 200A GeV Au + Au collision. Quark and hadronic matter contributions are shown separately. Right panel: p_T -integrated elliptic flow parameter for dileptons and various hadrons [93]

The p_T -integrated spectra and v_2 as a function of invariant mass M show well-defined peaks at the resonance masses (ρ , ω , and ϕ), as can be seen Fig. 27. For $M \leq M_\phi$, the dilepton spectrum is totally dominated by hadronic phase and above that it is dominated by contribution from QGP. $v_2(QM)$ is very small at large M and rises for smaller M . It shows a nature similar to the thermal photon v_2 . The M -dependent $v_2(HM)$ is significant only at the resonance masses and beyond ϕ mass its contribution to total v_2 is negligible. Thus, for large values of M or at early times flow comes from QGP phase and its value is very small, whereas at later times or at low M values it is from HM, which is very strong. The measurement of flow parameter at high M and/or high p_T values can be very useful to reveal a pure QGP signature.

5.3 Elliptic Flow of Decay Photons

We have already discussed that most of the produced photons in heavy-ion collisions are from the 2γ decay of π^0 and η mesons and the direct photons contain a small fraction of the inclusive photon spectrum. Thus it is very interesting to know the

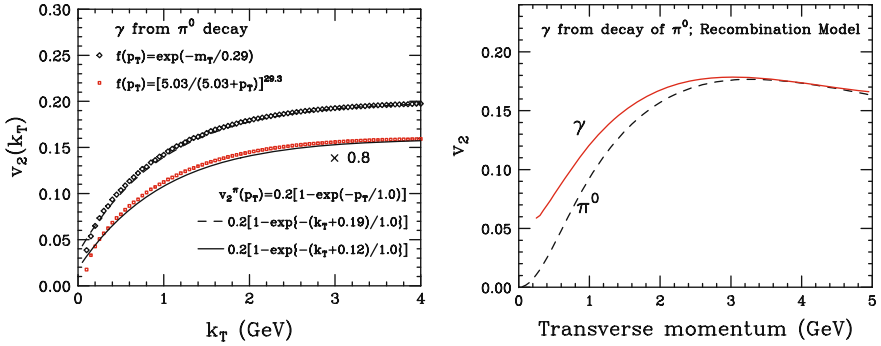


Fig. 28 *Left panel:* Elliptic flow of photons from π^0 decay at midrapidity. $f(p_T)$ stands for the momentum distribution of the π^0 . *Right panel:* Elliptic flow parameters for photons from decay of π^0 obtained using the recombination model (taken from [96])

nature of v_2 of decay photons from pion and η decays. The momentum distribution of decay photons from π^0 decay in an invariant form can be expressed as [94, 95]

$$k_0 \frac{dN}{d^3k}(p, k) = \frac{1}{\pi} \delta(p \cdot k - \frac{1}{2}m^2), \quad (56)$$

where p and k are the 4-momentum of the pion and photons and m is the pion mass. Thus the Lorentz invariant cross section of the decay photons using the decay kinematics from Eq. (56) is

$$k_0 \frac{d\sigma}{d^3k} = \int \frac{d^3p}{E} \left(E \frac{d\sigma}{d^3p} \right) \frac{1}{\pi} \delta(p \cdot k - \frac{1}{2}m^2). \quad (57)$$

Layek et al. [74] have calculated elliptic flow of decay photons considering several azimuthally asymmetric pion distributions (Fig. 28). They have shown that k_T -dependent v_2 of decay photons closely follows the $v_2(p_T)$ of π^0 evaluated at $p_T \sim k_T + \delta$ (where $\delta \sim 0.1\text{--}0.2$ GeV). Similar results were obtained for decay photons from η mesons also. This study could be useful in identifying additional sources of photons as the v_2 of π^0 is similar to that of π^+ and π^- . Also by using the property of quark number scaling or the recombination model, the decay photon v_2 can help to estimate the v_2 of constituent partons in the π^0 or η mesons (right panel of Fig. 28). See [96] for details.

5.3.1 Experimental Measurement of Direct Photon v_2

PHENIX has measured direct photons and its v_2 by subtracting v_2 of decay photons (2γ decay of π^0 and η mesons) from inclusive photon v_2 using appropriate weight factor [97]. The procedure followed by them to estimate direct photon v_2 is as follows:

$$v_2^{\text{dir.}} = \frac{R \times v_2^{\text{incl.}} - v_2^{\text{bkgd.}}}{R - 1}, \quad (58)$$

where R is the direct photon excess over hadron decays defined as

$$R = \frac{(\gamma/\pi^0)_{\text{incl.}}}{(\gamma/\pi^0)_{\text{bkgd.}}} \quad (59)$$

The factor R is measured from spectral analysis. The inclusive and hadron decay v_2 are measured using reaction plane method where the background photons are measured using a Monte Carlo simulation. We have already seen that the photon v_2 shows different signs and/or magnitude depending on the production procedure of photons in heavy-ion collisions. Thus experimental measurement of photon v_2 can be a very powerful tool to disentangle the intermix contributions from different sources in different p_T ranges. However, the experimentally measured preliminary PHENIX data still contain a large systematic error (Fig. 29), which need to be reduced before making any specific conclusion about direct photon v_2 .

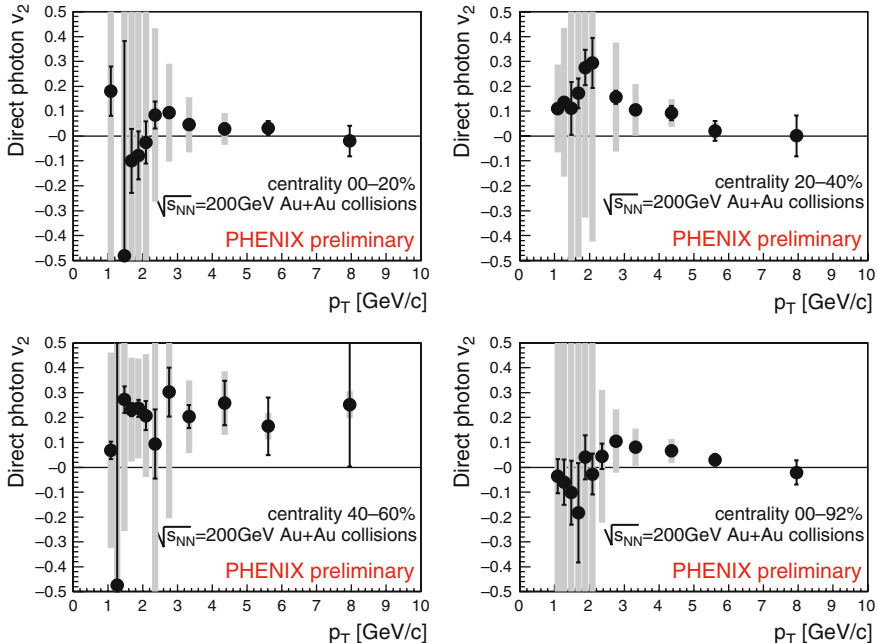


Fig. 29 Elliptic flow of direct photons from 200A GeV Au + Au collision at RHIC [98]

6 Photon-Tagged Jets

Jets are hard phenomenon characterized by a large momentum transfer between partons and are characterized by several hadrons in a small angle around a leading particle as a result of jet fragmentation. The hadrons surrounding a jet are known as associated particles of the jet.

One of the key observables at RHIC energy is the strong suppression of leading hadron yield at high values of transverse momentum compared to expectations based on $p + p$ or $d + A$ collisions at same collision energy. This is the celebrated phenomenon of “jet quenching.” It is assumed that the hard partons lose a large fraction of their energy when passing through the strongly interacting medium. A variety of qualitatively different models are available using collisional energy loss and radiative energy loss mechanisms to describe the nuclear modification factor R_{AA} defined as

$$R_{AA}(p_T, y) = \frac{d^2N_{AA}/dp_T dy}{T_{AA}(b)d^2\sigma_{NN}/dp_T dy}. \quad (60)$$

Here, T_{AA} is the nuclear overlap function and σ_{NN} is the nucleon–nucleon cross section. The major problem for studying jet properties arises from the fact that conventional calorimetric study cannot measure the jet energy loss very accurately. Also it is very difficult to directly measure the modification of jet fragmentation function and jet production cross section.

The “jet quenching” in heavy-ion collisions can be studied by measuring the p_T distributions of charged hadrons in opposite direction of a tagged direct photon. Quark–gluon Compton scattering and quark–antiquark annihilation process are the main mechanisms by which direct photons are produced at very high p_T , and jets are produced in the opposite direction of these photons. From momentum conservation law, the initial transverse energy of the produced jets are equal to that of the produced photons, i.e., $E_\gamma = E_{\text{jet}}$. Thus uncertainties regarding the jet cross section can be avoided by tagging a direct photon in the direction opposite to the jet (see [99]).

Medium-modified parton fragmentation function $D_{h/a}(z)$ (z is fractional momenta of the hadrons) is used to study the jet energy loss. The differential p_T distribution of hadrons from jet fragmentation in the kinematical region ($\Delta\phi$, Δy) using $D_{h/a}(z)$ can be written as

$$\frac{dN_{\text{ch}}^{\text{jet}}}{dy d^2p_T} = \sum_{r,h} r_a(E_T^\gamma) \frac{D_{h/a}(p_T/E_T)}{p_T E_T} \frac{C(\Delta y \Delta\phi)}{\Delta y \Delta\phi}, \quad (61)$$

where $C(\Delta y \Delta\phi) = \int_{|y| \leq \Delta y/2} dy \int_{|\phi - \bar{\phi}_\gamma| \leq \Delta\phi/2} d\phi f(y - |\phi - \bar{\phi}_\gamma|)$ is an overall factor and $f(y, \phi)$ is the hadron profile around the jet axis and $r_a(E_T^\gamma)$ is the fractional production cross section of a typical jet associated with the direct photons. Thus, comparison between extracted fragmentation function in AA and pp collisions can

be used to determine the jet energy loss as well as the interaction mean free path in the dense matter produced in high-energy heavy-ion collisions. Thorston Renk [100] has shown that by γ hadron correlation measurement, the averaged probability distributions for quarks are accessible experimentally and he has also explained an analysis procedure capable of distinguishing between different energy-loss scenarios leading to the same nuclear suppression factor (see Fig. 30).

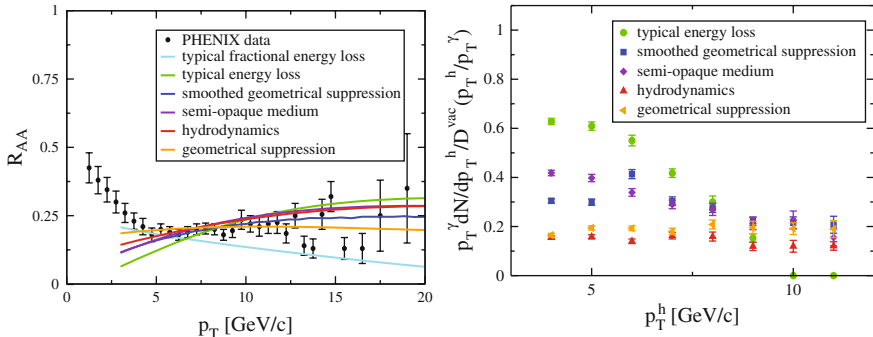


Fig. 30 *Left panel:* Nuclear suppression factor R_{AA} for different toy models and hydrodynamical simulation compared with PHENIX data. *Right panel:* Momentum spectrum of hard hadrons correlated back to back with a photon trigger normalized to the expectation of geometrical absorption (taken from [100])

6.1 Isolating the Bremsstrahlung Photons

In order to measure direct photon cross section by suppressing the hadron decay background or in particular to isolate bremsstrahlung photons from accompanying hadrons, an interesting method known as “isolation cut” can be used successfully. The basic assumption for performing the cut is that the hadronic energy in a cone around the photon is less than a certain fraction of the photon energy, i.e., a photon is considered as isolated if the combined energy of the accompanying hadrons is less than ϵE_γ (where E_γ is the photon energy) inside a cone of half-opening angle δ around the photon. The parameter ϵ is very small (~ 0.1) and is called the energy resolution parameter. The cone around the tagged photon is known as isolation cone. The cone opening can be related to the radius R of a circle centered around the photon in the center of mass system, where R is defined in terms of rapidity η and azimuthal angle ϕ as

$$R \geq \sqrt{\Delta\eta^2 + \Delta\phi^2}. \quad (62)$$

For small rapidities, the half-opening angle δ equals the radius R . This method was successfully implemented into the theoretical study of isolated prompt photon production considering fragmentation contribution also in next-to-leading order (NLO)

by Gordon and Vogelsang [28]. A very good accuracy of this method over a wide range of isolation parameters for prompt photon production was demonstrated in their calculation. Results from RHIC and LHC for this would be very valuable.

6.2 Dilepton-Tagged Jets

In the study of photon-tagged jets, the main problem arises from the jet pair production background, where a leading π^0 in the jet is misidentified as a photon. For an event having a huge background “isolation cut” is not a very efficient mechanism in the low p_T range to study photon-tagged jets in heavy-ion collisions and it is useful only for pp collisions. In the high p_T range although the background contribution related problems are reduced, a substantial problem in photon isolation is created by small opening angle. On the contrary jets tagged by dileptons are not affected by background and can be used to observe p_T imbalance, a signal of medium-induced partonic energy loss. As we have mentioned earlier, for dileptons not only p_T but also invariant mass M is another equally important parameter which can be used accordingly to study dilepton-tagged jets in the medium. At high p_T and high M , the dilepton yield is much lower compared to low p_T and low M range; however, the relative background contribution is also lower in that range.

At very high transverse momentum Drell–Yan process ($h_1 + h_2 \rightarrow l^+l^- + X$) dominates the dilepton production from QGP phase. Srivastava et al. [101] have estimated the results for dilepton-tagged jets by studying Drell–Yan process at NLO in relativistic heavy-ion collisions at RHIC and LHC energies. They have also shown that correlated charm and bottom decay are unimportant as background for dileptons having large transverse momentum or in the kinematical region of interest for jet quenching. Lokhtin et al. [102] have studied the dimuon + jet production (including both $\gamma^*/Z \rightarrow \mu^+\mu^-$ modes) at LHC energy and have shown the p_T imbalance between $\mu^+\mu^-$ pair and a leading particle in a jet is clearly visible even for moderate energy loss. It is directly related to absolute value of partonic energy loss and almost insensitive to the angular spectrum of emitted gluons and to experimental jet energy resolution.

7 Intensity Interferometry of Thermal Photons

The quantum statistical interference between identical particles emitted in relativistic heavy-ion collisions provide valuable insight about the shape and size of the particle emitting source. We know that direct photons emitted from different stages of the collision dominate the p_T spectra depending on the range of transverse momentum range. Thus, one can extract space–time dimension of the system at different stages of the collision by measuring the correlation radii for photons at different transverse momentum.

Two particle correlation function $C(\mathbf{q}, \mathbf{K})$ for photons having momenta \mathbf{k}_1 and \mathbf{k}_2 emitted from a completely chaotic source can be written as

$$C(\mathbf{q}, \mathbf{K}) = 1 + \frac{1}{2} \frac{|\int d^4x S(x, \mathbf{K}) e^{i\mathbf{q}\cdot\mathbf{x}}|^2}{\int d^4x S(x, \mathbf{k}_1) \int d^4x S(x, \mathbf{k}_2)}. \quad (63)$$

In the above equation, the factor 1/2 appears for averaging over spin and $S(x, \mathbf{K})$ is the space-time density function defined as

$$E \frac{dN}{d^3K} = \int d^4x S(x, \mathbf{K}), \quad (64)$$

$$\text{where } \mathbf{q} = \mathbf{k}_1 - \mathbf{k}_2, \mathbf{K} = (\mathbf{k}_1 + \mathbf{k}_2)/2. \quad (65)$$

The correlation function $C(\mathbf{q}, \mathbf{K})$ can be expressed in terms of outward, sideward, and longitudinal momentum difference and radii (q_{out} , q_{side} , q_{long} , and R_{out} , R_{side} , R_{long} , respectively) as

$$C(q_{\text{out}}, q_{\text{side}}, q_{\text{long}}) \sim 1 + \frac{1}{2} \exp[-(q_{\text{out}}^2 R_{\text{out}}^2 + q_{\text{side}}^2 R_{\text{side}}^2 + q_{\text{long}}^2 R_{\text{long}}^2)/2]. \quad (66)$$

Photon 4-momentum in terms of transverse momentum k_T , rapidity y , and azimuthal angle ψ can be expressed as

$$k^\mu = (k_T \cosh y, k_T \cos \psi, k_T \sin \psi, k_T \sinh y) \quad (67)$$

and

$$q_{\text{long}} = |k_{1z} - k_{2z}| = |k_{1T} \sinh y_1 - k_{2T} \sinh y_2|$$

$$q_{\text{out}} = |\mathbf{q}_T \cdot \mathbf{k}_T|/k_T,$$

$$q_{\text{side}} = |\mathbf{q}_T - q_{\text{out}} \mathbf{k}_T/k_T|.$$

Photon interferometry in the QGP phase has been investigated by several theoretical groups and the first experimental results on direct photon were obtained by WA98 [103] collaboration. Bass, Müller, Srivastava [6–9] have calculated two-body quantum correlation of high-energy photon using parton cascade model (PCM) and ideal hydrodynamic model for central 200A GeV Au + Au collision at RHIC. They have shown that one can differentiate between the direct photons from early pre-equilibrium stage and the same from later QGP and hadronic gas stages depending on features of the correlation function. Left panel of Fig. 31 shows that about 88% of the total photons having transverse momenta (1 ± 0.1) GeV (produced by hard parton scattering in PCM [104]) are emitted within a time period of 0.3 fm/c at rapidity $y = 0$. Right panel of the same figure shows that at $k_T = 1$ GeV, the contribution of pre-equilibrium phase and thermal photons is similar to the total photon yield, whereas at $k_T = 2$ GeV hard photons from PCM outshine the thermal ones by an order of magnitude. The emission time in PCM is very small and hydrodynamic calculation with $\tau_0 = 0.3$ fm/c allows a smooth continuation of the emission rate. Intensity correlation for $k_T \geq 2$ GeV (Fig. 31) reveals a pre-thermal photon

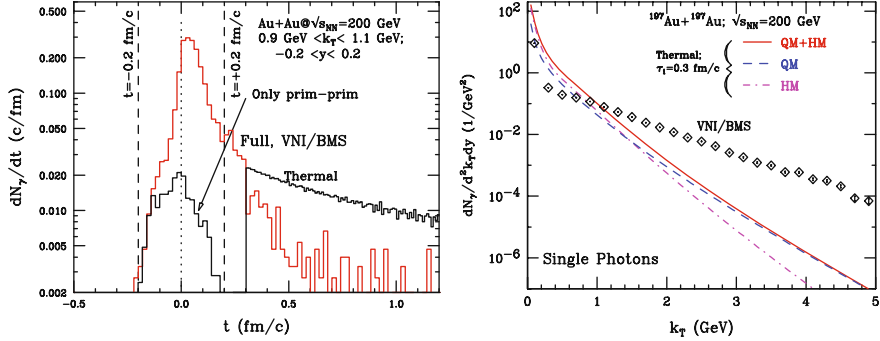


Fig. 31 *Left panel:* The production rate (per event) of hard photons in a central collision of gold nuclei at $\sqrt{s_{NN}} = 200$ GeV as a function of time in the centre of mass system. *Right panel:* Spectrum of photons from various sources. QM and HM denote quark matter and hadronic matter contribution respectively (figures are from [6–9])

dominated small size source of brief duration. On the contrary, for $k_T = 1$ GeV we can see much larger radii for an extended source and suppression of pre-thermal contribution over thermal (Fig. 32).

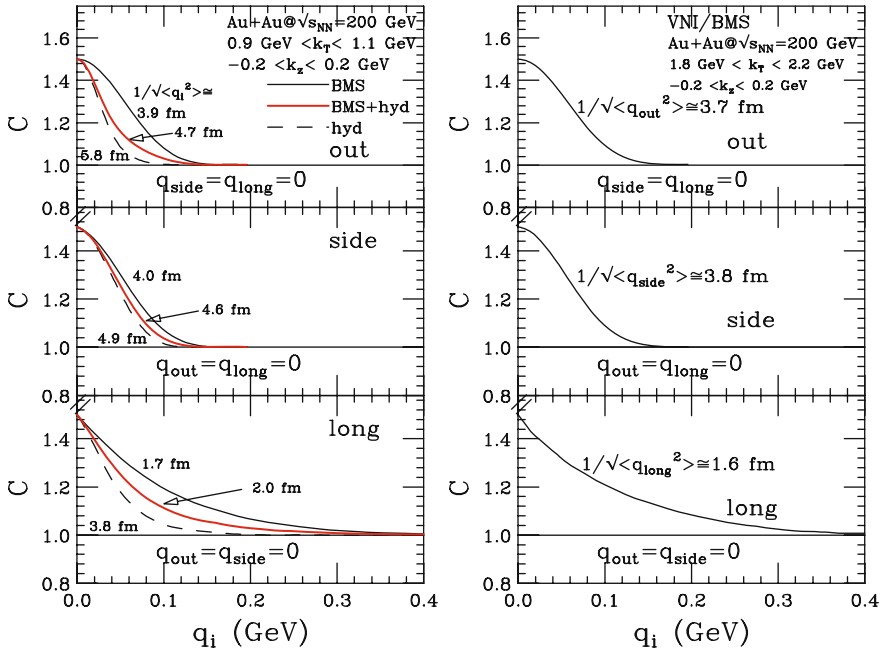


Fig. 32 *Left panel:* Intensity correlation of photons at 1 GeV, considering only PCM(BMS), only thermal (hyd), and all PCM + thermal photons (BMS+hyd) (See [6]). *Right panel:* The outward, sideward, and longitudinal correlations of direct photon predicted by PCM at $K_T = 2$ GeV, inclusion of thermal photons changes the results only marginally

Intensity interferometry of thermal photons having transverse momentum $k_T \sim 0.1 - 2.0$ GeV [55] provides an accurate information about the temporal and spatial structure of the interacting medium.

In reference [55] WA98 data are compared with theoretical results and prediction are given for RHIC and LHC energies. One-dimensional correlation function in terms of q_{inv} (invariant momentum difference) for different k_T and rapidity windows along with WA98 data is shown in Fig. 33. Theoretical results are well fitted in the form $C = 1 + 0.5 a \exp[-q_{inv}^2 R_{inv}^2 / 2]$ and are in reasonable agreement with the experimental data. At RHIC energy, contribution from quark matter increases and as a result the two-source aspect in the outward correlation radii becomes more clear. Similar results are obtained for LHC energies. It is found that the transverse momentum dependence of the different radii are quite different from the corresponding results for pions and do not decrease as $1/\sqrt{m_T}$. For SPS, RHIC, and LHC energies the longitudinal correlations show similar values, which can be explained as a result of boost invariance of the flow pattern.

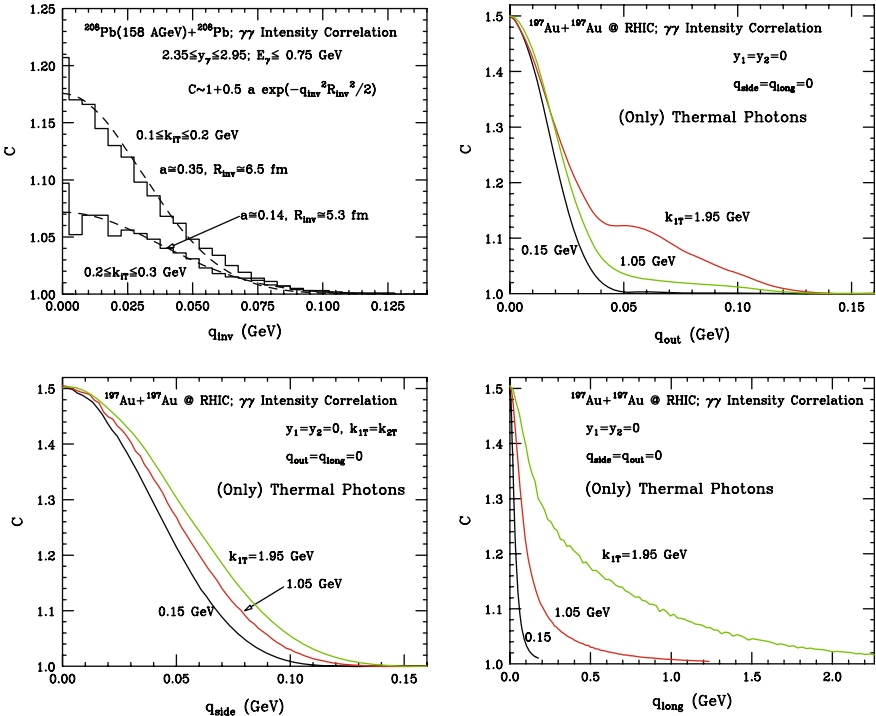


Fig. 33 One-dimensional correlation function for the kinematic window used in WA98 experiment, assuming a fully source and emitting only a single photon. Outward, sideward, and longitudinal correlation function for thermal photons in central collision at RHIC energy (taken from [55])

8 Epilogue

We have tried to give a reasonably complete introduction to the exciting possibilities provided by radiation of direct photons and dileptons for the study of the dynamics of relativistic heavy-ion collisions.

While low-mass dileptons provide insights into the medium modification of vector mesons, those having intermediate masses carry signatures of thermal radiation from the quark–gluon plasma. We have, due to lack of space, left out the discussion of correlated decay of charm and bottom mesons which give a large contribution to dileptons. These are also important as they carry valuable information about the extent of thermalization, elliptic flow, and energy loss exhibited by heavy quarks.

We have discussed sources of direct photons, consisting of prompt photons, thermal radiation from quark and hadronic matter, and those due to passage of jets through QGP. We have also seen that photons carry information about the initial temperature, evolution of elliptic flow, and size of the system. High statistics data at RHIC and LHC along with photon or dilepton-tagged jets will go a long way in seeing that we realize the full potential of electromagnetic probes of quark–gluon plasma.

Acknowledgments This write-up is based on the notes taken by RC and LB from the lectures given by DKS at the QGP Winter School 2008 at Jaipur. We thank the organizers for their warm hospitality. The work discussed here has benefited from discussions and collaborations with colleagues over many years and from many countries, and we take this opportunity to thank all of them and also to apologize to those whose work may not have found mention in these introductory lectures as this write-up is not intended to be a review.

Finally, we thank the organizers for their patience and for giving us extra time to complete this write-up.

References

1. B. Müller: *The Physics of Quark Gluon Plasma*, Springer, Heidelberg (1985) 219
2. C.Y. Wong: *Introduction of High Energy Heavy Ion Collisions*, World Scientific, Singapore (1994) 219, 232, 233, 243, 251
3. R.C. Hwa (ed.): *Quark Gluon Plasma*, vols. I and II, World Scientific, Singapore (1990 and 1995) 219
4. U. Heinz: CERN Yellow Report CERN-2004-001, arXiv: 0407360 [hep-ph] 219
5. E.L. Feinberg: Nuovo Cim. A **34**, 391 (1976) 220
6. S.A. Bass, B. Müller and D.K. Srivastava: Phys. Rev. Lett. **93**, 162301 (2004) 220, 259, 260
7. S.A. Bass, B. Müller and D.K. Srivastava: Phys. Rev. Lett. **90**, 082301 (2003)
8. S.A. Bass, B. Müller and D.K. Srivastava: Phys. Rev. C **66**, 061902 (2002)
9. T. Renk, S.A. Bass and D.K. Srivastava: Phys. Lett. B **632**, 632 (2006) 220, 259, 260
10. R. Chatterjee, E. Frodermann, U. Heinz and D.K. Srivastava: Phys. Rev. Lett. **96**, 202302 (2006) 220, 250, 251
11. U. Heinz, R. Chatterjee, E. Frodermann, C. Gale and D.K. Srivastava: Nucl. Phys. A **783**, 379 (2007) 220, 250, 251
12. R. Chatterjee and D.K. Srivastava: Phys. Rev. C **79**, 021901 (2009) 220
13. R.J. Fries, B. Müller and D.K. Srivastava: Phys. Rev. Lett. **90**, 132301 (2003) 220, 232, 240, 241

14. K. Kajantie, J. Kapusta, L. McLerran and A. Mekjian: Phys. Rev. **D 34**, 2746 (1986) 220, 244
15. M.M. Aggarwal et al. [WA98 Collaboration]: Phys. Rev. Lett. **85**, 3595 (2000) 221, 238
16. S.S. Adler et al. [PHENIX Collaboration]: Phys. Rev. Lett. **94**, 232301 (2005) 221, 239
17. S.S. Adler et al. [PHENIX Collaboration]: Phys. Rev. **C 76**, 034904 (2007) 222
18. A. Adare et al. [PHENIX Collaboration]: arXiv: 0804.4168 [nucl-ex] 223, 224
19. S. Bathe [PHENIX Collaboration]: Eur. Phys. J. **C 49**, 225 (2007) 223, 224
20. N.M. Kroll and W. Wada: Phys. Rev. **98**, 1355 (1955) 223
21. L.G. Landsberg: Phys. Rep. **128**, 301 (1985) 223
22. H. Gong [PHENIX Collaboration]: Proceedings of 19th International Conference on Ultra-Relativistic Nucleus-Nucleus Collisions: Quark Matter 2006 (QM2006), Shanghai, China, 14–20 Nov 2006, arXiv:0705.1133 [nucl-ex] 223, 224
23. T. Dahms et al.: Eur. Phys. J. **C 49**, 249 (2007) 223, 224
24. D.K. Srivastava: J. Phys. **G 35**, 104026 (2008) 224
25. P. Aurenche, J.-P. Guillet, E. Pilon and M. Werlen: Phys. Rev. **D 73**, 094007 (2006) 224, 225, 226
26. P. Aurenche, M. Fontannaz, J.-P. Guillet, B. Kniehl, E. Pilon and M. Werlen: Eur. Phys. J. **C 9**, 107 (1999) 225
27. L.E. Gordon and W. Vogelsang: Phys. Rev. **D 50**, 1901 (1994) 225
28. P. Aurenche, R. Basu, M. Fontannaz and R.M. Godbole: Eur. Phys. J. **C 42**, 43 (2005) 226, 258
29. S. Jeon, J. Jalilian-Marian and I. Sarcevic: Nucl. Phys. **A 715**, 795 (2003) 226
30. F. Arleo: JHEP **0609**, 015 (2006) 226
31. R. Chatterjee, D.K. Srivastava and S. Jeon: Phys. Rev. **C 79**, 034906 (2009) 227
32. T. Isobe [PHENIX Collaboration]: J. Phys. **G 34**, S1015 (2007) 227, 228, 240, 242
33. L.D. McLerran and T. Toimela: Phys. Rev. **D 31**, 545 (1985) 228
34. H.A. Weldon: Phys. Rev. **D 42**, 2384 (1990) 228
35. C. Gale and J. Kapusta: Nucl. Phys. **B 357**, 65 (1991) 228
36. J. Kapusta, P. Lichard and D. Seibert: Phys. Rev. **D 44**, 2774 (1991) 229, 231, 233, 234, 235, 236, 237
37. J. Kapusta, P. Lichard and D. Seibert: Phys. Rev. **D 47**, 4171 (1993) [Erratum] 229, 231, 233, 234, 235, 236
38. R. Baier, H. Nakagawa, A. Niegawa and K. Redlich: Z. Phys. **C 53**, 433 (1992) 229, 233
39. R.D. Pisarski: Nucl. Phys. **B 309**, 476 (1988) 231
40. R.D. Pisarski: Phys. Rev. Lett. **63**, 1129 (1989)
41. E. Braaten and R.D. Pisarski: Nucl. Phys. **B 337**, 569 (1990) 231
42. P. Arnold, G.D. Moore and L.G. Yaffe: JHEP **0112**, 009 (2001) 231, 236, 237
43. H. Nadeau: Phys. Rev. **D 48**, 3182 (1993) 232
44. S. Turbide, C. Gale, S. Jeon and G.D. Moore: Phys. Rev. **C 72**, 014906 (2005) 233
45. B.G. Zakharov: JETP Lett. **80**, 1 (2004) 233
46. L. Xiong, E.V. Shuryak and G.E. Brown: Phys. Rev. **D 46**, 3798 (1992) 236
47. C. Song: Phys. Rev. **C 47**, 2861 (1993) 236
48. J. Alam, P. Roy and S. Sarkar: Phys. Rev. **C 68**, 031901 (2003) 236
49. J. Alam, S. Sarkar, P. Roy, T. Hatsuda and B. Sinha: Ann. Phys. **286**, 159 (2001) 236
50. S. Turbide, R. Rapp and C. Gale: Phys. Rev. **C 69**, 014903 (2004) 236, 237, 239, 240
51. R. Albrecht et al. [WA80 Collaboration]: Phys. Rev. Lett. **76**, 3506 (1996) 237, 238
52. D.K. Srivastava and B. Sinha: Phys. Rev. Lett. **73**, 2421 (1994) 237, 238
53. J. Alam, D.K. Srivastava, B. Sinha and D.N. Basu: Phys. Rev. **D 48**, 1117 (1993) 237
54. R.C. Hwa and K. Kajantie: Phys. Rev. **D 32**, 1109 (1985) 237
55. D.K. Srivastava: Phys. Rev. **C 71**, 034905 (2005) 238, 261
56. A. Dumitru, U. Katscher, J.A. Maruhn, H. Stöecker, W. Greiner and D.H. Rischke: Phys. Rev. **C 51**, 2166 (1995) 238
57. N. Arbex, U. Ornik, M. Plümmer, A. Timmermann and R.M. Weiner: Phys. Lett. **B 345**, 307 (1995)
58. J. Sollfrank, P. Huovinen, M. Kataja, P.V. Ruuskanen, M. Prakash and R. Venugopalan: Phys. Rev. **C 55**, 392 (1997)
59. J.V. Steele, H. Yamagishi and I. Zahed: Phys. Rev. **D 56**, 5605 (1997)
60. T. Hirano, S. Muroya and M. Namiki: Prog. Theor. Phys. **98**, 129 (1997)

61. D.K. Srivastava and B.C. Sinha: Eur. Phys. J. **C 12**, 109 (2000)
62. D.K. Srivastava and B.C. Sinha: Eur. Phys. J. **C 20**, 397 (2001) [Erratum] 238
63. J. Cleymans, K. Redlich and D.K. Srivastava: Phys. Rev. **C 55**, 1431 (1997) 238, 239
64. D.K. Srivastava and B. Sinha: Phys. Rev. **C 64**, 034902 (2001) 238, 240
65. I. Kvasnikova, C. Gale and D.K. Srivastava: Phys. Rev. **C 65**, 064903 (2002) 239, 247, 248
66. J. Alam, S. Sarkar, T. Hatsuda, T.K. Nayak and B. Sinha: Phys. Rev. **C 63**, 021901 (2001) 239, 240
67. P. Huovinen, P.V. Ruuskanen and S.S. Rasanen: Phys. Lett. **B 535**, 109 (2002)
68. S.S. Rasanen: Nucl. Phys. **A 715**, 717 (2003)
69. H. Niemi, S.S. Rasanen and P.V. Ruuskanen: CERN Yellow Report, CERN-2004-009, arXiv:0311131 [hep-ph] 239
70. J. Alam, J.K. Nayak, P. Roy, A.K. Dutta-Mazumder and B. Sinha: J. Phys. **G 34**, 871 (2007)
71. D.G. d'Enterria and D. Peressounko: Eur. Phys. J. **C 46**, 451(2006) 240
72. B.B. Back et al. [PHOBOS Collaboration]: Phys. Rev. **C 65**, 061901 (2002) 241
73. J. Kapusta, L.D. McLerran and D.K. Srivastava: Phys. Lett. **B 283**, 145 (1992) 241
74. R.J. Fries, B. Müller and D.K. Srivastava: Phys. Rev. **C 72** 041902(R) (2005) 241, 254
75. S. Turbide, C. Gale, E. Frodermann and U. Heinz: Phys. Rev. **C 77**, 024909 (2008) 241, 242, 243, 251
76. H. Busching [PHENIX Collaboration]: Nucl. Phys. **A 774**, 103 (2006) 242
77. K. Kajantie, M. Kataja, L. McLerran and P.V. Ruuskanen: Phys. Rev. **D 34**, 811 (1986) 247
78. G. Agakichiev et al. [CERES Collaboration]: Eur. Phys. J. **C 41**, 475 (2005) 247, 248
79. D. Adamova et al. [CERES/NA45 Collaboration]: Phys. Rev. Lett. **91**, 042301 (2003) 247, 248
80. G.E. Brown and M. Rho: Phys. Rep. **269**, 333 (1996) 247
81. R. Rapp and J. Wambach: Eur. Phys. J. **A 6**, 415 (1999) 247
82. M. Masera et al.: Nucl. Phys. **A 590**, 93c (1995) 247
83. A.L.S. Angelis et al.: Eur. Phys. J. **C 13**, 433 (2000) 247
84. M.C. Abreu et al. [NA38/NA50 Collaboration]: Eur. Phys. J. **C 14**, 443 (2000) 247, 248
85. R. Rapp and E.V. Shuryak: Phys. Lett. **B 473**, 13 (2000) 247
86. R. Arnaldi et al. [NA60 Collaboration]: Phys. Rev. Lett. **96**, 162302 (2006) 249
87. H. van Hees and R. Rapp: Phys. Rev. Lett. **97**, 102301 (2006) 249
88. J. -Y. Ollitrault: Phys. Rev. **D 46**, 229 (1992) 249
89. U.W. Heinz and A. Kuhlman: Phys. Rev. Lett. **94**, 132301 (2005) 249
90. P.F. Kolb and U. Heinz: In: R.C. Hwa and X.-N. Wang (eds.) *Quark-Gluon Plasma 3*, World Scientific, Singapore (2004), arXiv: 0305084 [nucl-th] 249, 250
91. R. Chatterjee, D.K. Srivastava and U. Heinz: Proceedings of 20th International Conference on Ultra-Relativistic Nucleus-Nucleus Collisions: Quark Matter 2008 (QM2008), Jaipur, India, 4–10 Feb 2008 251, 252
92. R. Chatterjee, D.K. Srivastava and U. Heinz: Proceedings of International Conference on Particle and Nuclei (PANIC08), Eilat, Israel, 9–14 Nov 2008, arXiv: 0901.3270 [nucl-th] 251, 252
93. R. Chatterjee, D.K. Srivastava, U. Heinz and C. Gale: Phys. Rev. **C 75**, 054909 (2007) 252, 253
94. R.N. Cahn: Phys. Rev. **D 7**, 247 (1973) 254
95. C. Gale and J. Kapusta: University of Minnesota Report No. 88/2 (1988) [unpublished] 254
96. B. Layek, R. Chatterjee and D.K. Srivastava: Phys. Rev. **C 74**, 044901 (2006) 254
97. T. Sakaguchi [PHENIX Collaboration]: arXive: 0705.1711 [nucl-ex] 254
98. Kentaro Miki: Proceedings of 19th International Conference on Ultra-Relativistic Nucleus-Nucleus Collisions: Quark Matter 2006 (QM2006), Shanghai, China, 14–20 Nov 2006 255
99. X. -N. Wang, Z. Huang and I. Sarcevic: Phys. Rev. Lett. **77**, 231 (1996) 256
100. T. Renk: Phys. Rev. **C 74**, 034906 (2006) 257
101. D.K. Srivastava, C. Gale and T.C. Awes: Phys. Rev. **C 67**, 054904 (2003) 258
102. I.P. Lokhtin, A.V. Sherstnev and A.M. Snigirev: Phys. Lett. **B 599**, 260 (2004) 258
103. M.M. Aggarwal et al. [WA98 Collaboration]: Phys. Rev. Lett. **93**, 022301 (2004) 259
104. S. Turbide, C. Gale and R.J. Fries: Phys. Rev. Lett. **96**, 032303 (2006) 259